Direct imaging of shock wave splitting in diamond at Mbar pressure

Sergey Makarov,[1]* Sergey Dyachkov,[1] Tatiana Pikuz,[2] Kento Katagiri,[3,4] Hirotaka Nakamura[3], Vasily Zhakhovsky,[1] Nail Inogamov,[5] Victor Khokhlov,[5] Artem Martynenko,[1] Bruno Albertazzi,[6] Gabriel Rigon,[6,7] Paul Mabey,[6,8] Nicholas J Hartley,[9] Yuichi Inubushi,[10,11] Kohei Miyanishi,[11] Keiichi Sueda,[11] Tadashi Togashi,[10,11] Makina Yabashi,[10,11] Toshinori Yabuuchi,[10,11] Takuo Okuchi,[12] Ryosuke Kodama,[3,4] Sergey Pikuz,[1] Michel Koenig,[3,6] Norimasa Ozaki[3,4]

(1) *Joint Institute for High Temperatures of Russian Academy of Sciences, 13/2 Izhorskaya st., 125412 Moscow, Russia*
(2) *Institute for Open and Transdisciplinary Research Initiative, Osaka University, Suita, Osaka 565-0871, Japan*
(3) *Graduate School of Engineering, Osaka University, Suita, Osaka 565-0817, Japan*
(4) *Institute of Laser Engineering, Osaka University, Suita, Osaka 565-0871, Japan*
(5) *Landau Institute for Theoretical Physics of Russian Academy of Sciences, 1-A Akademika Semenova av., Chernogolovka, Moscow Region, 142432, Russia*
(6) *LULI, CNRS, CEA, École Polytechnique, UPMC, Univ Paris 06: Sorbonne Universités, Institut Polytechnique de Paris, F-91128 Palaiseau cedex, France*
(7) *Nagoya Univ, Grad Sch Sci, Chikusa Ku, Nagoya, Aichi 4648602, Japan*
(8) *Freie Universität Berlin, Department of Physics, Experimental Biophysics and Space Sciences, Arnimallee 14, 14195 Berlin, Germany*
(9) *SLAC National Accelerator Laboratory, 2575 Sand Hill Road, Menlo Park, CA 94025, USA*
(10) *Japan Synchrotron Radiation Research Institute, Sayo, Hyogo 679-5198, Japan*
(11) *RIKEN SPring-8 Center, Sayo, Hyogo 679-5148, Japan*
(12) *Institute for Integrated Radiation and Nuclear Science, Kyoto University, Yoshida-honmachi, Sakyo-ku, Kyoto 606-8501, Japan*

corresponding author: seomakarov28@gmail.com

Abstract

Understanding the behavior of matter at extreme pressures of the order of megabar (Mbar) is essential to gain insight into various physical phenomena at macro-scales ─ the formation of planets, young stars and cores of super-Earths, and at micro-scales ─ the damage ceramic materials and the high-pressure plastic transformation and phase transitions in solids. Under dynamic compression of solids up to Mbar pressures, even a solid with high strength exhibits plastic properties, causing the induced shock wave (SW) to split in two – elastic precursor and plastic SW. This phenomenon is described by theoretical models based on indirect measurements of material response. The advent of X-ray free-electron lasers (XFELs) made it possible to use their ultrashort pulses for direct observations of the propagation of shock waves in solid materials by the method of phase-contrast radiography. However, there is still a lack of comprehensive data for verification of theoretical models of different solids. Here, we present the results of an experiment in which the evolution of the coupled elastic-plastic wave structure in diamond was directly observed and studied with submicron spatial resolution, using the unique capabilities of the XFEL. The direct measurements allowed, for the first time, the fitting and validation of the 2D failure model for diamond in the range of several Mbar. Our experimental approach opens new possibilities for the direct verification and construction of equations of state of matter in the ultra-high stress range, which are relevant to solving a variety of problems in high energy density physics.

I. Introduction

Dynamic compression and shock loading of solid materials is a unique tool for the experimental study of the material response to ultrahigh strain rates and pressures[1,2]. A transition from the elastic to plastic response is produced with a rise in loading stress. The pressure P_{HEL} at the Hugoniot Elastic Limit (HEL), at which such a transition occurs is presented on the shock Hugoniot sketch shown in the left inset in Fig. 1. At the pressures $P > P_{HEL}$ the material is subjected to plastic strain. At this stage, the shock wave may split into a fast elastic wave (precursor) and a slower plastic wave that follows it [3–5]. The study of elastic-plastic shock waves is extremely important, especially in planetology and asteroid impacts. Indeed, all material properties (yield strength, Poisson's ratio, elastic and plastic waves structures and velocities) must be taken into account in numerical simulations of asteroid impact based on elastoplastic flow model. This is important to characterize the crater morphology (depth, diameter etc.) generated by the different waves and predict the consequence of an asteroid impact with Earth[6]. Separating and understanding the splitting mechanisms in shock wave induced plastic deformation in solids is of fundamental importance for developing accurate material models. One of the major problems in this field is the lack of accurate direct observational data to discriminate and validate models.

The most obvious and at the same time extremely difficult way to solve this problem is to directly visualize shock wave (SW) splitting in matter, and to resolve the elastic and plastic components. However, the splitting occurs at submicron scales, and the change in density, and hence contrast, with the waves is so low that it is impossible to do this using the traditional method of absorption radiography. To track shock wave evolution directly in visual observations, in particular elastic-plastic wave splitting in solids, it is necessary to use, firstly, lighting parallel to the wave front (see Fig. 1) and, secondly, the material must be transparent to the radiation used. Diamond is a common object in research of material response to high pressures [7–11], where the wave dynamics are analyzed in the direction normal to the shock front. This was either tracking the velocity of the diamond target boundary[7–10], on which the elastic wave first and then the plastic wave sequentially emerged from the volume of a crystal, or determining the reflectivity of the wave front[12]. However, in an extreme environment exceeding several Mbar, its physical characteristics are not well known even though diamond is used for high-pressure anvil cells (DACs[13,14]). A shock wave with pressures of several Mbars travels at speeds of few tens km/s, and it is necessary to observe the stress state of the lattice and its temporal change in real time. A broad and deep understanding of "diamond in the extreme environment" up to off-Hugoniot is required for improving DAC performance, the internal structure of giant planets, warm dense matter (WDM) characteristics, and the behavior of laser fusion fuel shells.

The methods which are conventionally used at high pressures, such as the Velocity Interferometer System for Any Reflector (VISAR)[4,15] and Photon Doppler Velocimetry (PDV)[4,16,17] can only probe a single surface and thus give only a limited idea of how shock waves behave inside a sample. Therefore, the state of matter as the shock wave propagates inside can only be assessed by an indirect method. Absorption and phase-contrast X-ray methods based on a laser-plasma source[18,19] give a low image contrast, which is not enough to clearly resolve the regions inside the shock wave or the plastic shock wave. Therefore, it is difficult to establish accurate equations of state and verify theoretical models for the response of a substance under ultrahigh pressure conditions.

The unique parameters of pulses generated by X-ray free electron lasers (XFELs) opened a new branch in the study of matter under ultrahigh pressures. In particular, femtosecond XFEL pulses began to be used in X-ray diffraction method (XRD) for measurement of shock-wave-driven twinning and lattice dynamics of solid[20] and the dynamic fracture of tantalum under extreme tensile stress[21]. There are two basic schemes for imaging with the XFEL probe using a focused and an unfocused beam. The first is a point projection scheme in which a magnified phase contrast image (PCI) is obtained by irradiation of sample from focusing point of the XFEL beam. This scheme is implemented at SLAC (MEC station) and at EuXFEL (MID station) [22–25]. Such an approach allows simultaneous investigation of the sample with PCI and XRD techniques with a single XFEL pulse [26]. In this scheme the spatial resolution is defined by linear magnification and resolution of detector. At the same time the field of view depends on the distance between focal point and the object. At present, a high spatial resolution has been achieved by applying great magnification leading to increasing the distance between the object and the detector up to a few meters. The second approach is more compact and allows it easier to adjust the position of the object to optimal PCI conditions without changing of the field of view [27,28]. In this scheme the spatial resolution is uniquely defined by the resolution of the detector. The first direct image of the shock wave into a solid using XFEL pulse was obtained in 2015 (work[22]), by combining a focused x-ray beam and a high-power laser. More recently, the first papers have appeared in which shock waves in silicon are visualized with the XFEL[29]. In these works, a point projection scheme was used to probe the matter.

Here we use an X-ray free-electron laser source to make comparisons between direct observation in experiment and hydrodynamic simulations of wave splitting into an elastic shock precursor and a plastic shock wave in diamond. We have used an phase-contrast imaging approach with unfocused XFEL probe beam and a lithium fluorine (LiF) fluorescent detector[27], which has been successfully applied in recent studies of microscale phenomena in plasma[28].

In the Sec. II of the article, a description of the experimental scheme is given, together with the analysis of phase-contrast images of laser-induced shock waves obtained in target. A description of the simulation methods used in this work, as well as the comparison of numerical results with experimental data and discussion are presented in Sec III. Our conclusions are presented in Sec. IV.

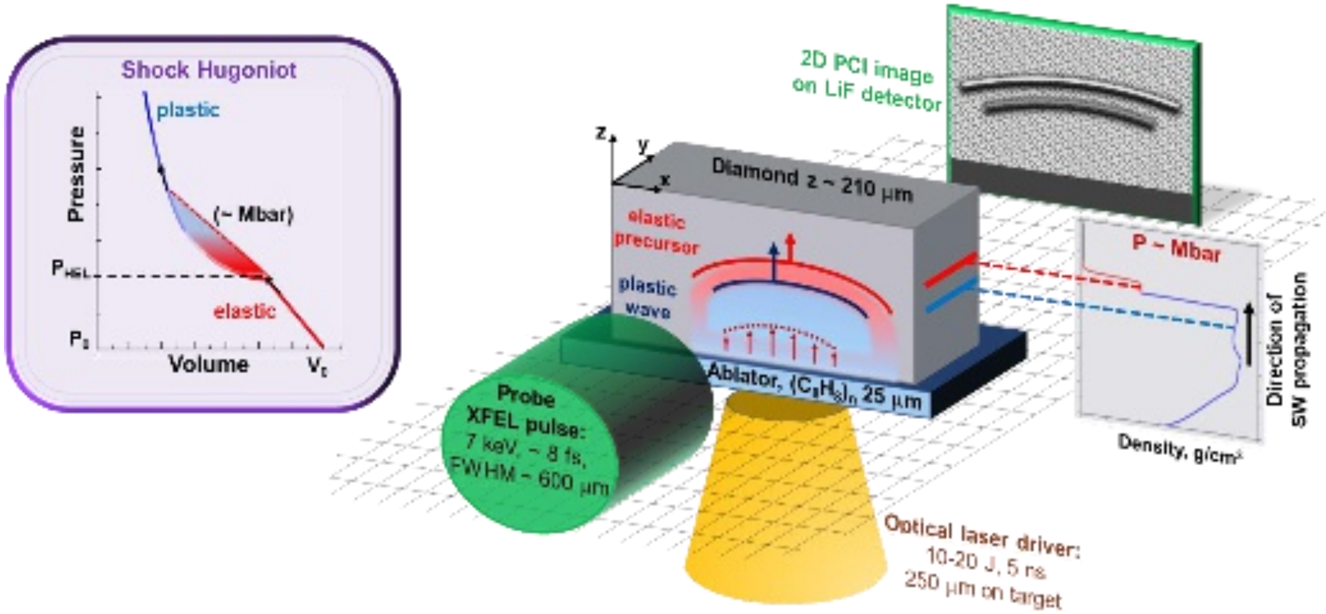

Fig. 1. Outline of pump-probe experiment for visualization of elastic-plastic shock waves (SW) evolution in diamond with submicron spatial resolution. A shock wave is driven by a focused drive laser (yellow) into the target consisting of an ablator (25 μm thick polystyrene) and a 210 μm thick monocrystalline diamond with crystallographic orientation <100> along the propagation direction of the laser. A 7 keV XFEL beam (green) probes the target with a delay of several nanoseconds with respect to the drive laser to observe the dynamics of the shock wave propagating in the diamond. A LiF detector was used to resolve the morphology of the low-contrast elastic-plastic shock waves with submicron spatial resolution.

II. Experimental results

A. Experimental setup

The experiment was performed at SPring-8 Angstrom Compact Free Electron Laser (SACLA XFEL, Japan) at experimental hutch EH5. A sketch of the experimental setup is shown in Fig. 1. The nanosecond optical driver pulse (laser wavelength 532 nm, pulse duration ~ 5 ns, pulse energy 10−20 J, full width at half maximum FWHM on sample 250 μm) focused in d_z direction on a multilayer target containing a thin layer of polystyrene ablator under the diamond sample and loaded it up to several Mbar pressures. The spatial and temporal profiles of the optical driver laser are shown in Fig.S1 (see Supplementary).

The multi-layer targets used for our experiments are composed of a polystyrene (1 g/cm^3) ablator and a monocrystalline type IIa diamond sample (3.51 g/cm^3) with dimensions of $\Delta x \times \Delta y \times \Delta z = 2000$ μm × 2000 μm × 25 μm and $\Delta x \times \Delta y \times \Delta z = 1500$ μm × 1500 μm × 210 μm respectively. Diamond crystallographic orientation is <100> along the shock direction (it corresponds also to the direction of a driver optical laser) and <010> along the XFEL irradiation direction. The diamond samples were made by chemical vapor deposition and both 1500 μm × 1500 μm surfaces were polished prior to the ablator being attached.

The evolution of the shock waves in the target was temporally resolved by irradiating the parallel XFEL beam (photon energy 7 keV, pulse energy 450 μJ, pulse duration 8 fs, divergence angle of ~ 2μrad, FWHM in the target plane 600 μm) in d_y direction with changing the delay relative to the optical drive laser irradiation timing, Fig.1. An ultra-short pulse duration of the XFEL beam provides a temporal resolution of the phase-contras imaging (PCI) platform in the femtosecond range (it corresponds to the pulse duration of the probe beam $\tau \sim 8$fs). A fluorescent crystal detector LiF was used to capture the phase-contrast pattern in $d_x \times d_z$ plane with a submicron spatial resolution. For this, it was placed ~ 110mm after the diamond sample, giving an optimal spatial resolution of 0.4μm in our experimental geometry (see Fig.S1, "Resolution and phase contrast approach" in Supplementary part). Note when the shock is launched within optical laser spot on sample, the shock propagates like a bubble into 3D space through the ablator. However, the XFEL probe projects the elastic-plastic regime of 3D over (d_x and d_z) directions together within the LiF image.

B. Observation of the shock waves propagation in diamond

The evolution of shock waves in the diamond sample was traced up to 12 ns after the beginning of the main laser pulse. In Fig. 2a we present a series of phase-contrast (PC) images recorded by using a LiF detector at different delay times in the range from 3 ns to 12 ns. Note that the images shown here are not from a single laser shot but instead from exposures with the same laser drive intensity ($I = 6 \times 10^{12}$ W/cm^2). The time at which the shock enters the diamond after the ablator has not been determined experimentally. To find this time, we simulated the interaction of the optical laser pulse with the ablator using a hydrodynamic code MULTI (see Sec.III-A). As a result, we calculated that the generated shock wave into the ablator reaches the diamond sample after 2.05 ns after the start of the laser pulse with $I = 6 \times 10^{12}$ W/cm^2. For comparison with experimental data, Figure 2b shows the calculation results of the shock waves evolution in diamond (details and conditions of the modeling as well as discussion are described in Section-III(B) below).

The PC enhancement and the submicron resolution of our experimental approach allowed us to clearly resolve the front of the generated shock waves, even though the difference in absorption between the shocked and unshocked regions of diamond was less than 0.5% (more details are shown in the Supplementary "Resolution and phase contrast approach"). In the region behind the plastic wave, the remaining trace of plastic deformations is visible.

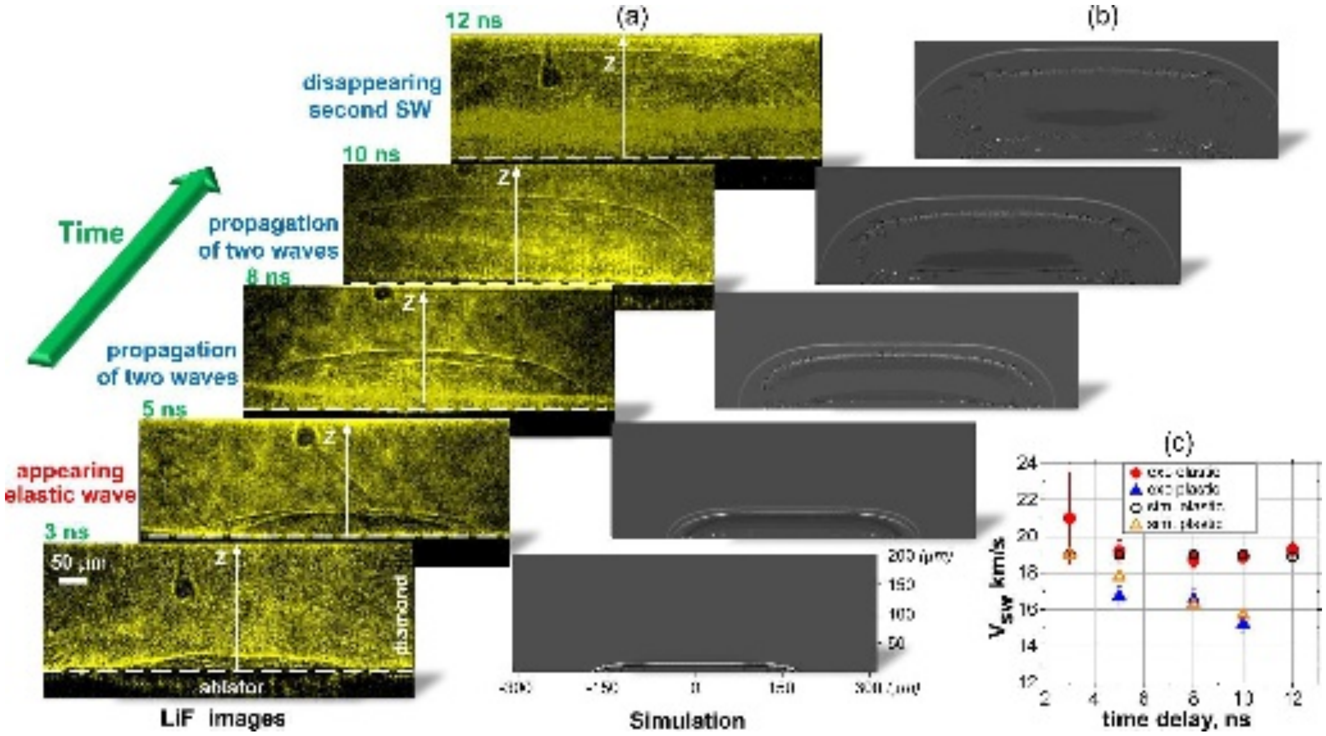

Fig. 2. Dynamics of shock wave evolution for times t = 3–12 ns after interaction of an optical laser with intensity I = 6×10^{12} W/cm^2 on the target: (a) Phase contrast images of SW evolution in diamond taken with a LiF detector located at a distance of 110 mm from the target. (b) Results of Smoothed-particle hydrodynamics (SPH) calculations in 2D geometry (strain rate map is shown). (c) SW velocities at different times revealed from the experimental LiF image (red and blue dots) and the SPH simulation (black and orange dots).

At the initial stage of waves evolution (t = 3 ns) one can observe only a single shock wave in Fig. 2a which indicates no noticeable wave splitting has occurred. At times between 3 ns < t < 5 ns, the shock wave splits into a clear two-wave structure in the diamond bulk due to the difference in elastic and plastic wave speeds[3]. Such a regime emerges because P_{HEL} is exceeded: a plastic wave appears and begins to propagate in the elastically compressed material with the bulk sound speed according to the equation of state, while the elastic precursor outruns such wave being enforced by shear stresses. The observed shock wave is supported by the laser pulse for several nanoseconds, after which the release wave propagating from the ablator side reduces the plastic wave amplitude. As a result, the plastic wave front disappears completely between 10 ns < t < 12 ns as shown in Fig.2a.

Using the data on the position of the shock wave fronts obtained from the radiographic LiF images, Fig. 2a, the velocities of the SWs observed in the experiment were reconstructed as they propagate inside the diamond. In Fig.2c, red and blue markers indicate the obtained velocities for elastic and plastic shock waves, respectively. It can be seen that the velocity of the precursor does not change as it passes through the diamond ($V_{elastic}$ = 19.0 ± 0.5 km/s), and is in good agreement with previous results from VISAR [4,11] and X-ray Imaging[22], as well as the longitudinal elastic sound wave speed in the <100> direction of diamond crystal[30]. At the same time, the plastic SW slows down (from $V_{plastic}$ = 21.0 ± 2.5 km/s to 15.2 ± 0.5 km/s) and disappears between 10-12 ns, Fig. 2a. This direct observation of plastic SW slowing is an important result for model validation, especially relative to VISAR, which only allows velocity evolution to be estimated by varying the target thickness, or calculating the velocity averaged over the entire transit. For example, previous work[11] measured the velocity of the plastic shock wave to be $V_{plastic}$ =13.64±0.39 km/s for the same loading conditions of a <100> oriented diamond sample, but this was limited to probing the velocity at the rear surface, and could not see possible changes in speed as the SW propagated.

III. Simulation results and discussion

In order to comprehensively investigate the state of matter under shock wave loading, it is necessary to know not only SW velocities, but also parameters such as pressure, density, ambient particle velocity, strain rate, and the bulk and shear modulus. Although the radiography images only allow us to measure the velocities of SW and to obtain the linear density map, other parameters can be revealed from the simulation. For this purpose, we performed a simulation of SW propagation inside the target.

Smoothed particle hydrodynamics (SPH) is widely used to model compressible media with strength at extremes. In such conditions, propagation of shock waves may be accompanied by the development of instabilities, formation of cavities, material spallation and fracture, which are difficult to model using the conventional Eulerian or Lagrangian methods on a mesh. Most Eulerian codes and the aforementioned Lagrangian MULTI code do not include material strength, which is necessary to model the splitting of elastic and plastic shock waves. The meshless SPH approach allows to model such phenomena naturally, without using complex algorithms for capturing the interfaces and the free boundaries, while its Lagrangian formulation leads to adaptation of particle sizes in accordance with the material strain.

The main reason for the application of the SPH for the problem here is its ability to model the intense loads of materials with strength. Diamond has a uniquely high HEL of 0.5 – 0.8 [Mbar] and is subjected to loads up to several Mbar in our experiments. However, our SPH implementation is lacking the radiation transport support, so firstly MULTI modeling of the polystyrene-diamond interface were performed to setup the appropriate boundary conditions.

A. Polystyrene response to the pump laser

Modelling of laser ablation and shock wave (SW) generation in polystyrene was performed using a one-dimensional radiation hydrodynamics code MULTI [31]. For the simulations, we used SESAME table No. 7590 for polystyrene (its gross chemical formula is $(C_8H_8)_n$) and SESAME table No. 7830 for diamond with initial densities of ρ_1 = 1.1 g/cm^3 and ρ_2 = 3.52 g/cm^3, respectively. The plastic thickness was set to 25μm.

Figure 3 shows the zt-diagrams as colormaps for the density and the pressure from a particular MULTI simulation. Shown are the hydrodynamic processes occurring in the target at time and space intervals of 1–5 ns and 20–50 μm, respectively. The position 0 μm corresponds to the ablator-diamond interface, while the “front” part of the ablator at which the laser pulse arrives at time 0 ns (1% of the maximum laser intensity) is placed at z = −25 μm.

The laser pulse (LP) is absorbed in the polystyrene ablator resulting in extreme heating and pressure growth. The ablated surface is evaporated and ionized producing plasma, so that LP continues to be absorbed in the area of the corona with a critical density (about 2 orders of magnitude lower than the value in solid ablator). LP of the intensity $I = 6\times10^{12}$ W/cm^2 produces the pressure in the corona of about 2 Mbar which keeps the bulk of the ablator from unloading until the end of LP. An initial shock wave propagates along the ablator to the interface with diamond: the ablator layer is compressed by ~ 3–3.5 times (its thickness changes from 25μm to ~ 6–8 μm) as the pressure increases to ~ 2 Mbar, which is close to the pressure at the laser ablation front as shown in Fig. 3 at 2–2.5 ns.

The shock wave reaches the interface between polystyrene and diamond at ~ 2.05 ns. The main shock wave begins to propagate through the diamond sample, while the reflected shock wave begins to propagate through the precompressed polystyrene moving in the opposite direction from the diamond boundary to the ablation front. This reflected shock wave passes the thin layer of the shocked ablator in 0.4 ns and reaches the ablation front. Afterwards, the SW is reflected by this boundary and produces the spray of rarefaction waves resulting in the ablator expansion. The rarefaction wave reaches the surface of the diamond at ~ 2.7 ns and follows the main shock wave in the diamond bulk.

One can note the “triangle” of high density in the ablator formed by the aforementioned shock wave which is reflected from the ablator-diamond interface, Fig.3a. The density in this triangle exceeds the initial density by 4.5–5 times producing the pressure about ~ 4 Mbar which is about 2 times higher than the pressure in the plasma at the ablation front, Fig.3b.

The release wave reaches the interface at ~ 2.7 ns which is less than the pulse duration (5 ns). This leads to the pressure drop from ~ 4 Mbar to the pressure of the laser corona (~ 2 Mbar) which sustains until the end of the laser pulse duration. The velocity of the ablator-diamond interface moves according to the applied pump: it accelerates up to ~ 7 km/s by 2.7 ns. The end of the laser pulse is followed by the gradual decrease of pressure in the ablated plasma. As a result, the unburnt part of the ablator begins to release and is pushed from the interface. The pressure on the diamond surface remains for a few tenths of nanoseconds until the “signal” about the end of the laser heating of the corona and zero pressure at the edge of the unburnt ablator reaches the diamond. The release leads to a gradual decrease of the interface velocity to almost 0 km/s.

The above mechanism is realized for laser pulse intensities starting from 10^{12} W/cm^2 and higher. For lower intensities of the order 10^{11} W/cm^2, the shock wave passing through the ablator reaches the ablator-diamond interface only after the end of the laser pulse.

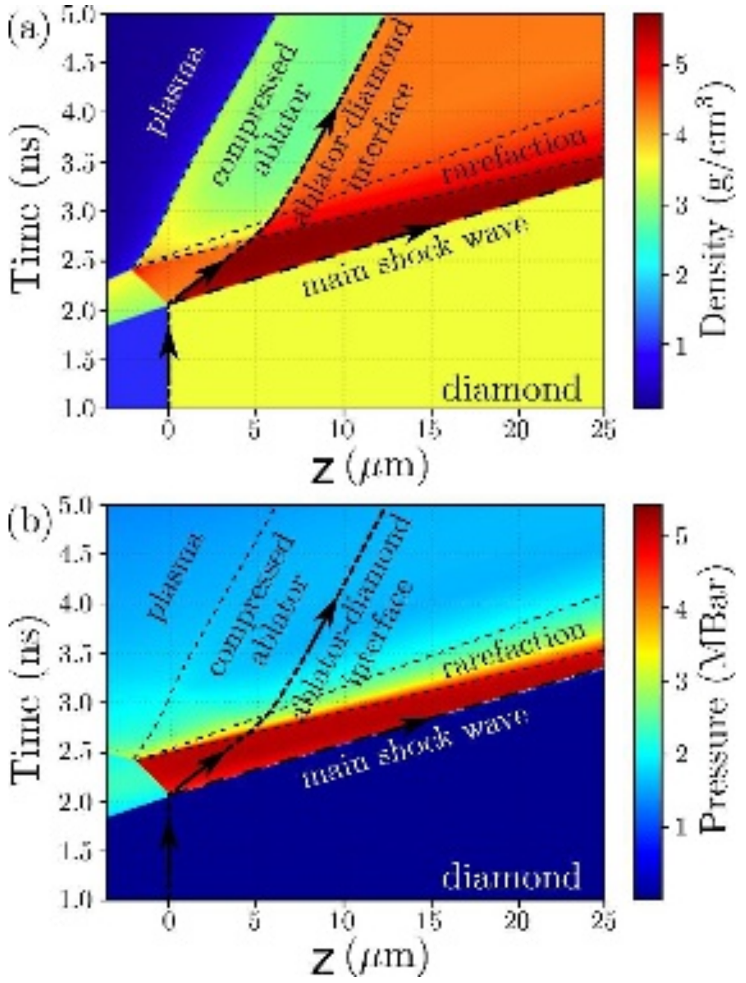

Fig. 3. (a) Density and (b) pressure maps obtained in the one-dimensional simulation using radiation hydrodynamics code MULTI.

The above simulations only consider a one-dimensional case, but in reality, there is spatial variation in the ablator-diamond interface velocity υ_P. The laser intensity in our experiments is supposed to have a super-gaussian distribution:

$$I(r) = I_0 \times \exp\left[\left(-\frac{e^2}{2{R_0}^2}\right)^3\right], \tag{1}$$

where $R_0 \simeq 125$ μm is the radius of a laser spot, r is the distance from its center and I_0 is the peak intensity.

To reproduce reasonably response of a multi-dimensional ablator we model the velocity $\upsilon_P(t)$ at various laser intensities $I \in (0, I_0]$ in one-dimensional MULTI code, which are interpolated for $\upsilon_P(t, I)$. The latter function is then transformed to $\upsilon_P(r, t) = \upsilon_P(t, I(r))$ and can be applied to model a multi-dimensional boundary condition at the ablator-diamond interface, if the transverse gradients of material velocity are notably smaller than the inwardly-directed normal gradient along z-direction.

Fig. 4(a-c) shows the result of MULTI profiles simulation and their interpolation. To construct $\upsilon_P(t, I)$ we calculated 10 interface velocity profiles in MULTI for the intensities $I \in [0.1,1,2,3,4,5,6,7,8,9] \times 10^{12}$ W/cm^2 as shown in Fig. 4a. As a result, the obtained interpolation $\upsilon_P(t, I)$ is shown in Figure 4(b,c). One may notice that the higher intensity pulses arrive at the ablator-diamond interface faster due to a dramatic change in the ablator sound velocity at high compression. The arrival of the shock from the ablator provides an extreme growth of velocity up to several km/s, which is followed by a small plateau and a gradual release.

The transition from the function $\upsilon_P(t,I)$ to $\upsilon_P(r,t)$ according to the distribution (1) is presented in Fig. 4d for several peak intensities I_0, where x is the axis directed along the spot diameter. One may notice the formation of the most intense load around the center of the spot, which is followed by the fast release. However, one may notice a ring at the periphery which produces some load after the release in the center due to later arrival of a peripheric shock wave. The latter is clearly seen for $I_0 = 3 \times 10^{12}$ W/cm^2 in Fig. 4d. It is unclear whether this effect is an artificial result of the interpolation, or it may appear in real simulation of 2D (3D) laser radiation absorption. Nevertheless, such small distortion at the periphery does not affect the propagation of a main shock wave in diamond as we can see from the following SPH simulation results.

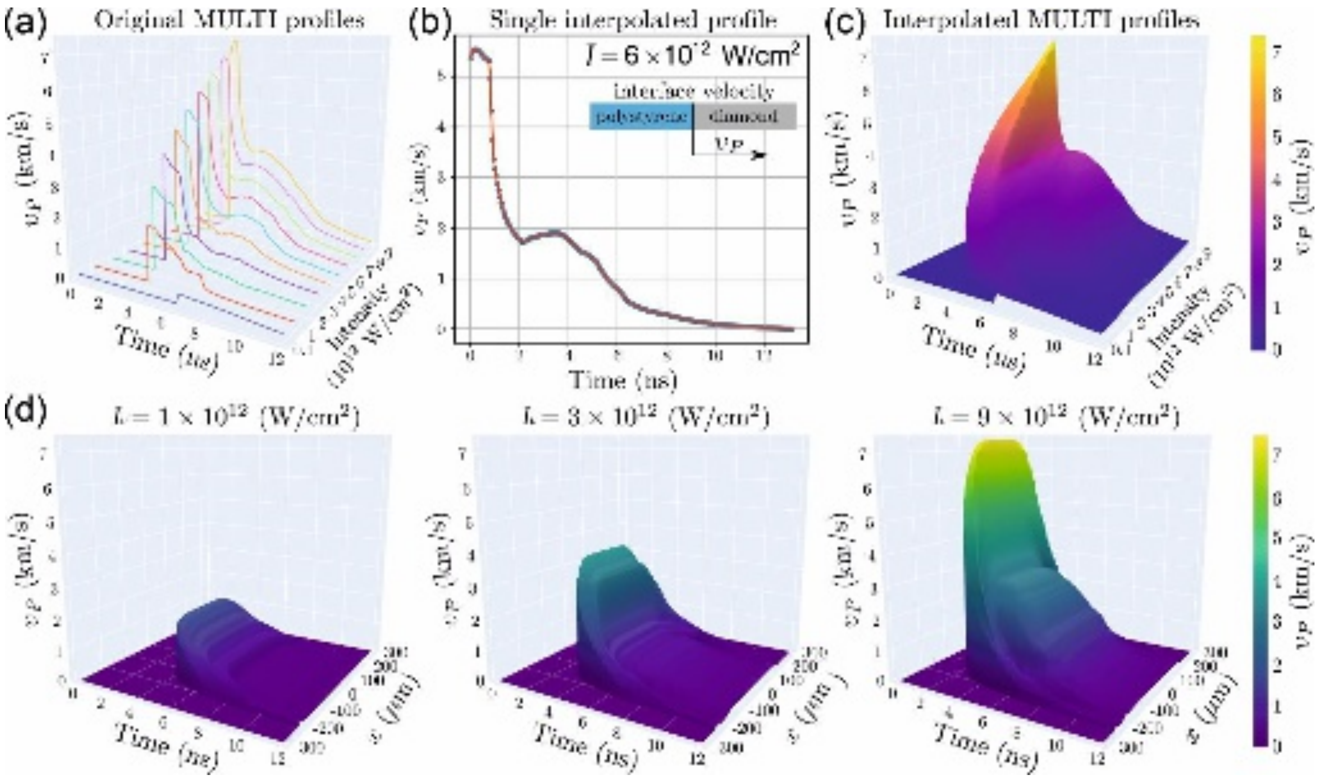

Fig. 4. (a) The velocity profiles $\upsilon_P(t)$ of the ablator-diamond interface obtained in 1D MULTI simulations for various intensities. (b,c) The result of the velocity profiles interpolation $\upsilon_P(t, I)$ required for further multi-dimensional SPH simulations with strength. (d) The velocity profiles $\upsilon_P(x, t)$ (x is the axis directed along the spot diameter) obtained according to the spatial laser intensity profile for different peak intensities $I_0 = 1 \times 10^{12}$ W/cm^2, $I_0 = 3 \times 10^{12}$ W/cm^2, $I_0 = 9 \times 10^{12}$ W/cm^2.

B. Failure model for diamond under shock loading

As has recently been shown [4,32], the models of metal plasticity are insufficient to describe the mechanical deformation of shock compressed diamond single crystals at stresses beyond the Hugoniot Elastic Limit. McWilliams et al.[11] note that diamond is a brittle material, the response of which is close to that of silicon carbide ceramics, which strength degrade because of material failure at shock loads above HEL. In our research we used the failure model [33] developed for strong ceramic materials such as boron carbide or silicon carbide. The model supposes that the strength of the intact material loaded to HEL begins to degrade with the plastic strain accumulation until the lower strength boundary (failed material strength) is reached. The shapes of the intact and failed material strength curves depending on pressure and strain rate guide the kinetics of the failure process.

The model parameters are first calibrated using the VISAR data on uniaxial shock compression of diamond crystal in the <100> direction provided by McWilliams et al. [11]. To obtain preliminary parameters of the failure model for diamond we performed numerical simulations of the tests dh2, dh9, and dh18 (Fig.S4 in the Supplementary). It is worth noting that our failure model is isotropic but being calibrated for the <100> direction it should be consistent with our XFEL observations. The impact in the experiments [11] is performed using the intense laser pulse applied to aluminum buffer, so that the impactor velocity is estimated according the velocity plateau achieved at maximum compression. The width and height of the elastic precursor and the kinetics of failure are adjusted by varying the Poisson ratio and the shape of the intact and failed material strength curves (in more details in the Supplementary “Diamond failure model”)

In the frame of failure model, the 1D and 2D simulations were performed with the Smoothed Particle Hydrodynamics (SPH) code[34] to model shock propagation in diamond induced by the ablated layer of polystyrene. The details of simulation description are presented in the Supplementary (“Continuum mechanics simulations”)**.** In Figure 2, the comparison of the experimental LiF images and 2D continuum mechanics simulation[35] is shown. The two-wave shock structure — an elastic precursor followed by an inelastic compression wave — is observed under loading of single-crystal diamond compressed to peak stresses up to ~ 3 Mbar. As can be seen in Fig. 2(a,b), the calculated SPH patterns successfully reproduce the appearance of an elastic precursor at time 3 ns $< t < 5$ ns and the disappearance of the plastic shock front at time 10 ns $< t < 12$ ns, which agrees with the experimental radiographic images. There is also a good agreement between the velocities of the observed waves, as seen in Fig. 2c. For convenience, the experimental shock fronts are indicated by dashed curves at the corresponding SPH results in Fig.5a. The density and pressure distribution along the Z direction are shown in Fig.5(b,c).

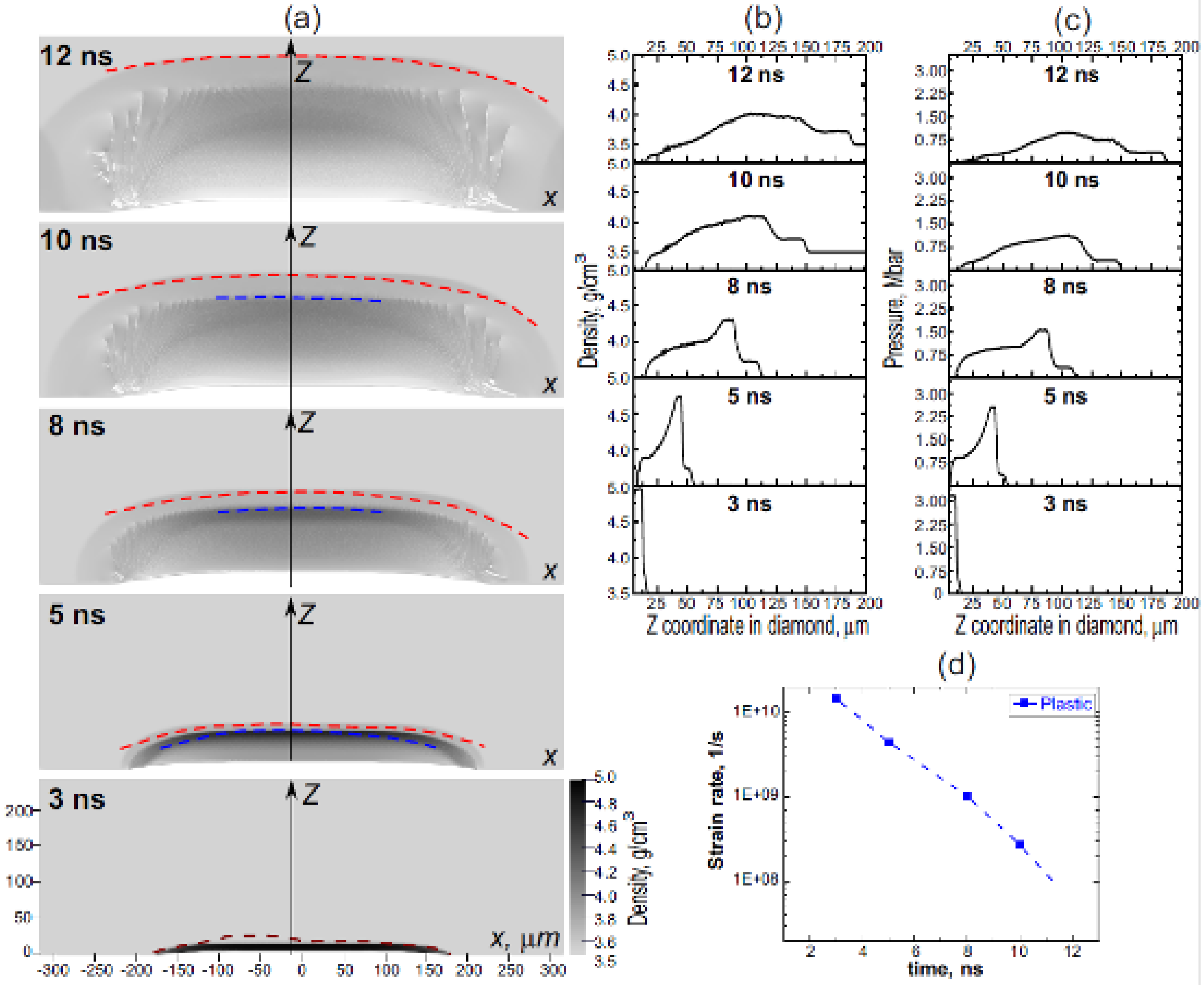

Fig. 5. Results of SPH simulations: (a)The two-dimensional maps of the density. The experimental shock fronts were digitized and placed as dashed red (elastic) and blue (plastic) curves at the corresponding SPH results with the failure model. (b) Density and (c) Pressure data retrieved along Z-axis in case (a). (d) Strain rate value for plastic SW revealed with SPH simulation.

As we saw in the experiments, the simulated elastic and plastic waves are not separated at 3 ns. The observed difference in the propagated distance at that time may happen due to non-uniform heating of the ablator which results in the wave front distortion. At 5 ns the separation of the elastic precursor is seen both in the experiment and simulation, and the observed and predicted wave speeds become close. At 8 ns, the waves have separated further, and the positions of simulated shock fronts agree well with the experiment. The rarefaction wave overtakes the plastic wave at about 10 ns, so that it almost disappears: the predicted position of the remaining part still agrees with the experiment. Finally, while the plastic wave disappeared at 12 ns, the elastic one continues to propagate further. It should be noted the presence of oblique lines that can be seen in the calculated density distributions in Fig.5a. These lines are the directions of destruction of the diamond under its loading.

The obtained correspondence is in agreement with the McWilliams et al. experiments [11], which used to fit the failure model of diamond. The best agreement between experimentally measured velocities and simulated ones is achieved by setting the yield strength to 0.7 Mbar and Poisson's ratio to 0.1 (see Supplementary "Diamond failure model" for more details). It should be also noted that by directly comparing the experiment with the simulation, it was found that the strain rate in the plastic wave dropped from $1.5*10^{10}$ s^{-1} to $5.6*10^{7}$ s^{-1}, Fig.5d.

The presented SPH simulation demonstrates the ability to reproduce the complex phenomena of waves splitting in the bulk of material sample. The series of experimental images can be used to adjust the strength model precisely by tracking positions of the shock fronts.

C. Estimation of density gradient in shock waves

As part of the study of shock wave morphology, we estimate a density gradient (width of shock wave fronts) using a method based on the analysis of monochromatic X-ray images with high spatial resolution in phase contrast. For this, we performed a simulation of the phase contrast images observed in the experiment to compare them with experimental data. The modeling of the phase contrast images was provided using the open-access software framework for coherent and partially coherent X-ray wavefront propagation simulations, WavePropaGator (WPG)[36]. The mathematical description used in WPG for modelling the propagation of XFEL radiation through composite targets is presented in detail in the paper [27]. We consider a probe of XFEL beam with the same initial parameters described in our article.

Images corresponding to times t = 3 ns (one SW is observed) and t = 8 ns (two SWs are clearly visible) were selected for analysis. To simulate the propagation of the SACLA beam through a shocked diamond sample, a number of independent parameters were introduced. These include the density of the compressed material, the density gradients of the shock waves and the SW density amplitudes (further details in the Supplementary "Estimation of density gradient in shock waves"). After setting up the incident beam and the transmission plane (target), we propagate the wavefront using a free space propagator over a distance of 110 mm to the observation plane (LiF detector). By fixing parameters retrieved from SPH simulations (density distribution in the diamond sample along the propagation direction SW, as shown in Fig. 5b) and by varying the density gradients of the shock waves at the fronts, we found the solutions describing the experimental PCI profiles for the time delays 3 ns and 8 ns. It was found that the width of the elastic-plastic structure at a time of 3 ns was 50 nm, while the width of the fronts at 8 ns was 40 nm and 70 nm for elastic and plastic shock waves, respectively, Fig.6. These estimates are an order of magnitude higher than the values expected by theory (of the order of the interatomic lattice spacing), which could be due to two reasons:

- we do not observe a flat front of the shock waves, but a curved one, which blurs the experimental profile of the phase contrast image.

- the detector resolution obviously increases the experimentally measured profile, which is then compared to the model.

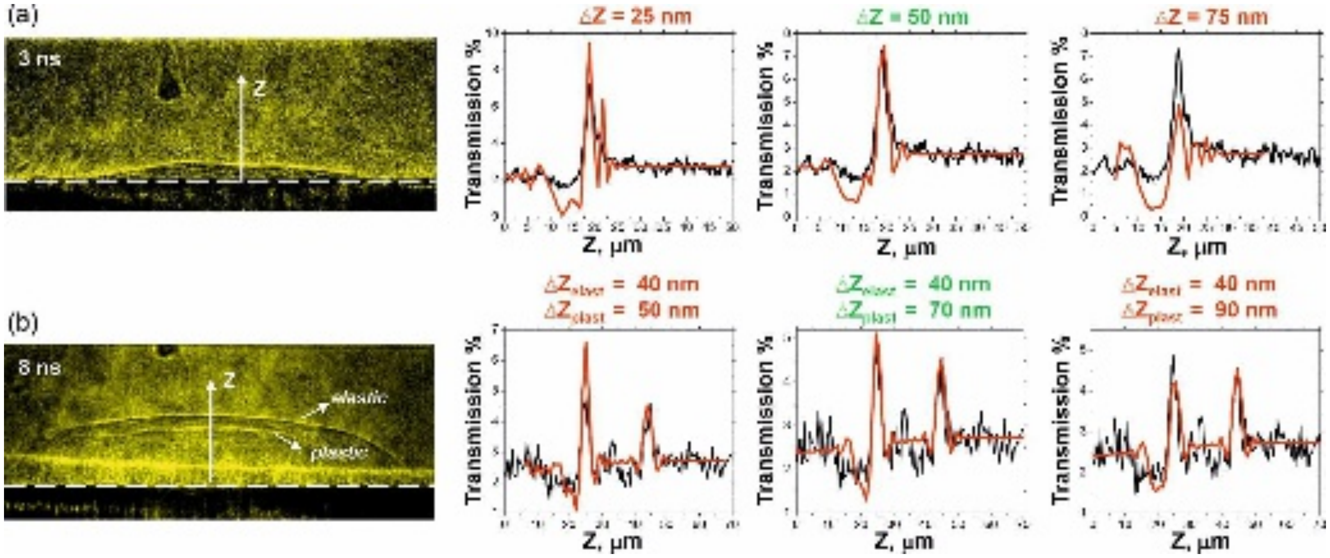

Fig. 6. Results of the estimation of the front width ΔZ of shock waves observed in diamonds at times t = 3 ns (a) and t = 8 ns (b). The left PC images show the areas where the intensity distribution was recorded for the experimental profile. The black and red lines in the right panel correspond to the experimental and simulated profiles traced along the Z direction, respectively.

D. Discussion

Several advantages of our experimental-theoretical approach compared to existing one should be mentioned as it can lead researchers to misunderstand their data:

- VISAR does not allow the measured velocities to be directly associated with specific waves. It is even worse when the material under study is opaque to visible light. The information are then transported to the rear surface of the sample, mixed and analysis is much more difficult (see for example ref[11]). In addition, it should be noted that the loss of stability of the surface of the test sample during melting can lead to a strong decrease in its reflectivity due to a strong shock wave effect, which limits the range of application of interferometric methods in the study of shock wave processes.
- In addition, the decrease of the plastic wave velocity observed in our work is a crucial parameter to benchmark the experimental data to numerical simulation and help to constrain the material properties (Yield strength, Poisson’s ratio).

The experimental scheme shown in this study allows us to overcome this difficulty as the two-wave structure is clear in our data. At first sight, the presence of a pair-wave structure in diamond pumped with a ~6 TW/cm^2 laser is in contradiction with the recent study by Schropp et al.[22], in which an experiment was performed with diamond at approximately twice the laser drive intensity. The propagation of a shock wave was recorded in phase-contrast images, but the splitting regime was not observed. To resolve this contradiction, we performed further SPH modelling using the diamond model calibrated with our experimental data, at the experimental conditions of Shropp et al.

Figure 7 shows the results of the 1D calculations, which show the presence of a plastic shock wave split from the elastic shock front at the early stage of wave evolution. The wave splitting is visible after 0.4 ns, but the plastic wave decays by 0.6 ns which makes it difficult to observe this phenomenon in study[22]. Our simulation shows that the intense damage emerging in the plastic wave after the intense loading introduces density fluctuations into the material. The plastic wave leaves a region of damaged material which corresponds to the trace of plastic deformations in the form of a dark zone with fixed width of 13-15 μm observed in the phase-contrast images[22]. The strain produced by the elastic wave is reversible, so that the diamond unloads to near-normal density. It should be noted, that this elastic wave gradually decays, but in Schropp's study[22] it is faster due to unloading from free boundaries of the sample, which is not accounted for in our 1D simulation. Nevertheless, the wave speed observed in simulation agrees well with the shock velocity V = (19.9 ± 1.7) km/s measured in their study[22].

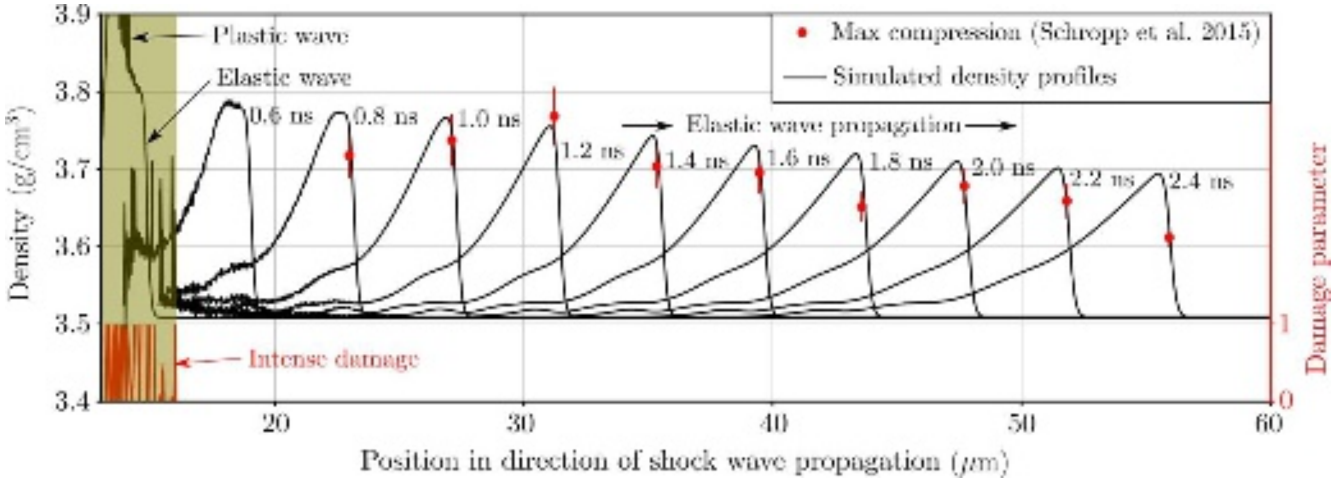

Fig. 7. Shock wave profiles in diamond under laser intensity ~ 1.2×10^{13} W/cm^2 used in work [22]**:** the experimental data for maximal compression detected during shock propagation is placed at positions calculated with the fixed shock speed V = 20.6 km/s (within the range 19.9 ± 1.7 km/s[22]). The 1D SPH simulation performed using the diamond model calibrated with our experimental data which also agrees with Schropp's data[22]. SPH reveals the existence of plastic wave at early times which should completely decay by 0.6 ns, so that it could not be detected in Schropp's experiments[22].

IV. Conclusion

In the present paper, we make significant step further implementing phase-contrast approach by using unfocused XFEL probe beam and at the first-time direct resolve the splitting of shock wave into an elastic precursor and plastic SW in diamond. We succeeded in tracing the evolution of the structure from the moment of appearance of the elastic precursor up to the stage of disappearing of the plastic shock wave with a submicron resolution as well as the remaining trace of plastic deformations. A single direct measurement allows to validate a strength model for diamond in the range of several Mbar. The excellent agreement achieved between the experimental data and continuum mechanics modelling shown in our work not only paves the way for direct measurement of the dynamic yield strength of materials as a function of strain rate, but also highlights the usefulness of these facilities for the study of high-speed crack dynamics and unusual stress-induced solid-state phase transitions. This combined experimental-theoretical approach opens new horizons in the development of models and validation of pressure-driven shock wave simulations. This goes well beyond EOS measurements using VISAR, by observing continuous evolution of the two-wave structure and evolution throughout the depth of the target, allowing much more information about the processes to be extracted, and giving direct comparison with simulated data.

ACKNOWLEDGMENTS

We thank the technical staff of SACLA for their support during the experiments. The experiments were performed at BL3 of SACLA with the approval of the Japan Synchrotron Radiation Research Institute (proposal Nos. 2021A8004 and 2021B8002). The high-power drive laser installed in SACLA EH5 was developed with the corporation of Hamamatsu Photonics. The installation of Diffractive Optical Elements (DOE) to improve the smoothness of the drive laser-pattern was supported by the SACLA Basic Development Program.

FUNDING:

The work was carried out with the financial support of the Russian Federation represented by the Ministry of Science and Higher Education of the Russian Federation (grant No. 075-15-2021- 1352). This work was supported by KAKENHI (grant no. 17K05729 and no. 21K03499) from the Japan Society for the Promotion of Science (JSPS).

AUTHOR DECLARATIONS

Conflict of Interest

The authors have no conflicts to disclose.

Author contributions:

NO and MK conceived the project. TP, HN, GR, BA, PM, MK, NH, KK, YI, KM, KS, TT, MY, TY, TO and NO performed the experiment. MULTI simulation was performed by AM. SPH simulation was performed by SD. WavePropaGator simulation was performed by SM. SM analyzed the experimental data and interpreted the experimental results with SD, TP, SP, VZ, NI, RK and VK. The paper was written by SM and SD. All co-authors commented on the manuscript.

DATA AVAILABILITY:

All data are available in the main text or the supplementary materials. The data that support the findings of this study are available from the corresponding authors upon request. The SPH, MULTI, and WavePropagator codes used for this study are available on reasonable request to serj.dyachkov@gmail.com, martynenko.art@gmail.com and seomakarov28@gmail.com respectively.

References

[1] T.S. Duffy, R.F. Smith, Ultra-high pressure dynamic compression of geological materials, Front. Earth

Sci. 7 (2019) 1–20. https://doi.org/10.3389/feart.2019.00023.

[2] S. Brygoo, E. Henry, P. Loubeyre, J. Eggert, M. Koenig, B. Loupias, A. Benuzzi-Mounaix, M. Rabec Le Gloahec, Laser-shock compression of diamond and evidence of a negative-slope melting curve, Nat. Mater. 6 (2007) 274–277. https://doi.org/10.1038/nmat1863.

[3] G.I. Kanel, V.E. Fortov, S. V. Razorenov, Shock-Wave Phenomena and the Properties of Condensed Matter, Springer, New York, 2004, n.d. https://doi.org/10.1007/978-1-4757-4282-4.

[4] J.M. Winey, M.D. Knudson, Y.M. Gupta, Shock compression response of diamond single crystals at multimegabar stresses, Phys. Rev. B. 101 (2020) 184105. https://doi.org/10.1103/PhysRevB.101.184105.

[5] S.J. Turneaure, P. Renganathan, J.M. Winey, Y.M. Gupta, Twinning and Dislocation Evolution during Shock Compression and Release of Single Crystals: Real-Time X-Ray Diffraction, Phys. Rev. Lett. 120 (2018) 265503. https://doi.org/10.1103/PhysRevLett.120.265503.

[6] G.S. Collins, H.J. Melosh, R.A. Marcus, Earth Impact Effects Program: A Web-based computer program for calculating the regional environmental consequences of a meteoroid impact on Earth, Meteorit. Planet. Sci. 40 (2005) 817–840. https://doi.org/10.1111/j.1945-5100.2005.tb00157.x.

[7] D.G. Hicks, T.R. Boehly, P.M. Celliers, D.K. Bradley, J.H. Eggert, R.S. McWilliams, R. Jeanloz, G.W. Collins, High-precision measurements of the diamond Hugoniot in and above the melt region, Phys. Rev. B - Condens. Matter Mater. Phys. 78 (2008) 174102. https://doi.org/10.1103/PhysRevB.78.174102.

[8] M.D. Knudson, M.P. Desjarlais, D.H. Dolan, Shock-Wave Exploration of the High-Pressure Phases of Carbon, Science (80-.). 322 (2008) 1822–1825. https://doi.org/10.1126/science.1165278.

[9] J.H. Eggert, D.G. Hicks, P.M. Celliers, D.K. Bradley, R.S. McWilliams, R. Jeanloz, J.E. Miller, T.R. Boehly, G.W. Collins, Melting temperature of diamond at ultrahighpressure, Nat. Phys. 6 (2010) 40–43. https://doi.org/10.1038/nphys1438.

[10] R.F. Smith, J.H. Eggert, R. Jeanloz, T.S. Duffy, D.G. Braun, J.R. Patterson, R.E. Rudd, J. Biener, A.E. Lazicki, A. V. Hamza, J. Wang, T. Braun, L.X. Benedict, P.M. Celliers, G.W. Collins, Ramp compression of diamond to five terapascals, Nature. 511 (2014) 330–333. https://doi.org/10.1038/nature13526.

[11] R.S. McWilliams, J.H. Eggert, D.G. Hicks, D.K. Bradley, P.M. Celliers, D.K. Spaulding, T.R. Boehly, G.W. Collins, R. Jeanloz, Strength effects in diamond under shock compression from 0.1 to 1 TPa, Phys. Rev. B - Condens. Matter Mater. Phys. 81 (2010) 27–36. https://doi.org/10.1103/PhysRevB.81.014111.

[12] K. Jakubowska, D. Mancelli, R. Benocci, J. Trela, I. Errea, A.S. Martynenko, P. Neumayer, O. Rosmej, B. Borm, A. Molineri, C. Verona, D. Cannatà, A. Aliverdiev, H.E. Roman, D. Batani, Reflecting laser-driven shocks in diamond in the megabar pressure range, High Power Laser Sci. Eng. 9 (2021) e3. https://doi.org/10.1017/hpl.2020.38.

[13] H.K. Mao, High-Pressure Physics: Sustained Static Generation of 1.36 to 1.72 Megabars, Science (80-.). 200 (1978) 1145–1147. https://doi.org/10.1126/science.200.4346.1145.

[14] B. Li, C. Ji, W. Yang, J. Wang, K. Yang, R. Xu, W. Liu, Z. Cai, J. Chen, H. kwang Mao, Diamond anvil cell behavior up to 4 Mbar, Proc. Natl. Acad. Sci. U. S. A. 115 (2018) 1713–1717. https://doi.org/10.1073/pnas.1721425115.

[15] L.M. Barker, The development of the VISAR, and its use in shock compression science, 11 (2000) 11–18. https://doi.org/10.1063/1.1303413.

[16] O.T. Strand, D.R. Goosman, C. Martinez, T.L. Whitworth, W.W. Kuhlow, Compact system for high-speed velocimetry using heterodyne techniques, Rev. Sci. Instrum. 77 (2006). https://doi.org/10.1063/1.2336749.

[17] T. Ao, D.H. Dolan, Effect of window reflections on photonic Doppler velocimetry measurements, Rev. Sci. Instrum. 82 (2011). https://doi.org/10.1063/1.3551954.

[18] F. Barbato, S. Atzeni, D. Batani, D. Bleiner, G. Boutoux, C. Brabetz, P. Bradford, D. Mancelli, P. Neumayer, A. Schiavi, J. Trela, L. Volpe, G. Zeraouli, N. Woolsey, L. Antonelli, Quantitative phase contrast imaging of a shock-wave with a laser-plasma based X-ray source, Sci. Rep. 9 (2019) 1–11. https://doi.org/10.1038/s41598-019-55074-1.

[19] L. Antonelli, S. Atzeni, D. Batani, S.D. Baton, E. Brambrink, P. Forestier-Colleoni, M. Koenig, E. Le Bel, Y. Maheut, T. Nguyen-Bui, M. Richetta, C. Rousseaux, X. Ribeyre, A. Schiavi, J. Trela, X-ray absorption radiography for high pressure shock wave studies, J. Instrum. 13 (2018) 1–8. https://doi.org/10.1088/1748-0221/13/01/C01013.

[20] C.E. Wehrenberg, D. McGonegle, C. Bolme, A. Higginbotham, A. Lazicki, H.J. Lee, B. Nagler, H.S. Park, B.A. Remington, R.E. Rudd, M. Sliwa, M. Suggit, D. Swift, F. Tavella, L. Zepeda-Ruiz, J.S. Wark, In situ X-ray diffraction measurement of shock-wave-driven twinning and lattice dynamics, Nature. 550 (2017) 496–499. https://doi.org/10.1038/nature24061.

[21] B. Albertazzi, N. Ozaki, V. Zhakhovsky, A. Faenov, H. Habara, M. Harmand, N. Hartley, D. Ilnitsky, N. Inogamov, Y. Inubushi, T. Ishikawa, T. Katayama, T. Koyama, M. Koenig, A. Krygier, T. Matsuoka, S. Matsuyama, E. McBride, K.P. Migdal, G. Morard, H. Ohashi, T. Okuchi, T. Pikuz, N. Purevjav, O. Sakata, Y. Sano, T. Sato, T. Sekine, Y. Seto, K. Takahashi, K. Tanaka, Y. Tange, T. Togashi, K. Tono, Y. Umeda, T. Vinci, M. Yabashi, T. Yabuuchi, K. Yamauchi, H. Yumoto, R. Kodama, Dynamic fracture of tantalum under extreme tensile stress, Sci. Adv. 3 (2017) 1–7. https://doi.org/10.1126/sciadv.1602705.

[22] A. Schropp, R. Hoppe, V. Meier, J. Patommel, F. Seiboth, Y. Ping, D.G. Hicks, M.A. Beckwith, G.W. Collins, A. Higginbotham, J.S. Wark, H.J. Lee, B. Nagler, E.C. Galtier, B. Arnold, U. Zastrau, J.B. Hastings, C.G. Schroer, Imaging Shock Waves in Diamond with Both High Temporal and Spatial Resolution at an XFEL, Sci. Rep. 5 (2015) 1–8. https://doi.org/10.1038/srep11089.

[23] B. Nagler, A. Schropp, E.C. Galtier, B. Arnold, S.B. Brown, A. Fry, A. Gleason, E. Granados, A. Hashim, J.B. Hastings, D. Samberg, F. Seiboth, F. Tavella, Z. Xing, H.J. Lee, C.G. Schroer, The phase-contrast imaging instrument at the matter in extreme conditions endstation at LCLS, Rev. Sci. Instrum. 87 (2016). https://doi.org/10.1063/1.4963906.

[24] D.S. Hodge, A.F.T. Leong, S. Pandolfi, K. Kurzer-Ogul, D.S. Montgomery, H. Aluie, C. Bolme, T. Carver, E. Cunningham, C.B. Curry, M. Dayton, F.-J. Decker, E. Galtier, P. Hart, D. Khaghani, H. Ja Lee, K. Li, Y. Liu, K. Ramos, J. Shang, S. Vetter, B. Nagler, R.L. Sandberg, A.E. Gleason, Multi-frame, ultrafast, x-ray microscope for imaging shockwave dynamics, Opt. Express. 30 (2022) 38405. https://doi.org/10.1364/oe.472275.

[25] J. Hagemann, M. Vassholz, H. Hoeppe, M. Osterhoff, J.M. Rosselló, R. Mettin, F. Seiboth, A. Schropp, Johannes Möller, Jörg Hallmann, C. Kim, M. Scholz, U. Boesenberg, R. Schaffer, A. Zozulya, W. Lu, R. Shayduk, A. Madsen, C.G. Schroera, T. Salditt, Single-pulse phase-contrast imaging at free-electron lasers in the hard X-ray regime, J. Synchrotron Radiat. 28 (2021) 52–63.

https://doi.org/10.1107/S160057752001557X.

[26] F. Seiboth, L.B. Fletcher, D. McGonegle, S. Anzellini, L.E. Dresselhaus-Cooper, M. Frost, E. Galtier, S. Goede, M. Harmand, H.J. Lee, A.L. Levitan, K. Miyanishi, B. Nagler, I. Nam, N. Ozaki, M. Rödel, A. Schropp, C. Spindloe, P. Sun, J.S. Wark, J. Hastings, S.H. Glenzer, E.E. McBride, Simultaneous 8.2 keV phase-contrast imaging and 24.6 keV X-ray diffraction from shock-compressed matter at the LCLS, Appl. Phys. Lett. 112 (2018). https://doi.org/10.1063/1.5031907.

[27] A.Y. Faenov, T.A. Pikuz, P. Mabey, B. Albertazzi, T. Michel, G. Rigon, S.A. Pikuz, A. Buzmakov, S. Makarov, N. Ozaki, T. Matsuoka, K. Katagiri, K. Miyanishi, K. Takahashi, K.A. Tanaka, Y. Inubushi, T. Togashi, T. Yabuuchi, M. Yabashi, A. Casner, R. Kodama, M. Koenig, Advanced high resolution x-ray diagnostic for HEDP experiments, Sci. Rep. 8 (2018). https://doi.org/10.1038/s41598-018-34717-9.

[28] G. Rigon, B. Albertazzi, T. Pikuz, P. Mabey, V. Bouffetier, N. Ozaki, T. Vinci, F. Barbato, E. Falize, Y. Inubushi, N. Kamimura, K. Katagiri, S. Makarov, M.J.E. Manuel, K. Miyanishi, S. Pikuz, O. Poujade, K. Sueda, T. Togashi, Y. Umeda, M. Yabashi, T. Yabuuchi, G. Gregori, R. Kodama, A. Casner, M. Koenig, Micron-scale phenomena observed in a turbulent laser-produced plasma, Nat. Commun. 12 (2021) 2679. https://doi.org/10.1038/s41467-021-22891-w.

[29] S.B. Brown, A.E. Gleason, E. Galtier, A. Higginbotham, B. Arnold, A. Fry, E. Granados, A. Hashim, C.G. Schroer, A. Schropp, F. Seiboth, F. Tavella, Z. Xing, W. Mao, H.J. Lee, B. Nagler, Direct imaging of ultrafast lattice dynamics, Sci. Adv. 5 (2019). https://doi.org/10.1126/sciadv.aau8044.

[30] S.F. Wang, Y.F. Hsu, J.C. Pu, J.C. Sung, L.G. Hwa, Determination of acoustic wave velocities and elastic properties for diamond and other hard materials, Mater. Chem. Phys. 85 (2004) 432–437. https://doi.org/10.1016/j.matchemphys.2004.02.003.

[31] R. Ramis, R. Schmalz, J. Meyer-Ter-Vehn, MULTI — A computer code for one-dimensional multigroup radiation hydrodynamics, Comput. Phys. Commun. 49 (1988) 475–505. https://doi.org/10.1016/0010-4655(88)90008-2.

[32] J.M. Lang, J.M. Winey, Y.M. Gupta, PHYSICAL REVIEW B 97 , 104106 (2018) Strength and deformation of shocked diamond single crystals : Orientation dependence, Phys. Rev. B. 97 (2018) 104106. https://doi.org/10.1103/PhysRevB.97.104106.

[33] S.A. Dyachkov, A.N. Parshikov, M.S. Egorova, S.Y. Grigoryev, V. V. Zhakhovsky, S.A. Medin, Explicit failure model for boron carbide ceramics under shock loading, J. Appl. Phys. 124 (2018). https://doi.org/10.1063/1.5043418.

[34] M.S. Egorova, S.A. Dyachkov, A.N. Parshikov, V. V. Zhakhovsky, Parallel SPH modeling using dynamic domain decomposition and load balancing displacement of Voronoi subdomains, Comput. Phys. Commun. 234 (2019) 112–125. https://doi.org/10.1016/j.cpc.2018.07.019.

[35] A.N. Parshikov, S.A. Medin, Smoothed Particle Hydrodynamics Using Interparticle Contact Algorithms, J. Comput. Phys. 180 (2002) 358–382. https://doi.org/10.1006/jcph.2002.7099.

[36] L. Samoylova, A. Buzmakov, O. Chubar, H. Sinn, WavePropaGator : interactive framework for X-ray free-electron laser optics design and simulations, J. Appl. Crystallogr. 49 (2016) 1347–1355. https://doi.org/10.1107/S160057671600995X.

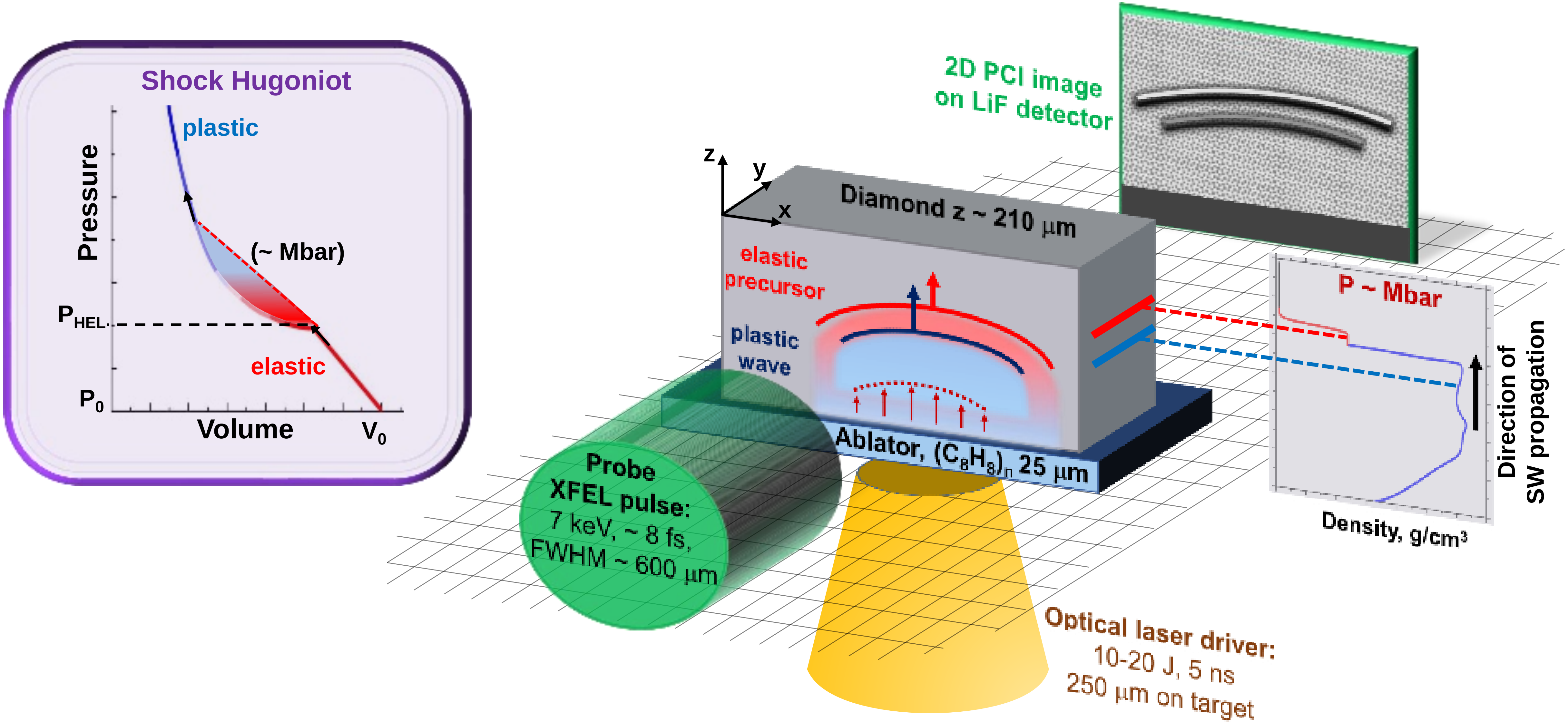
Shock Hugoniot
Pressure
plastic
(~ Mbar)
P_{HEL}
elastic
P_0
Volume
V_0
2D PCI image
on LiF detector
z
y
x
Diamond z ~ 210 μm
elastic
precursor
plastic
wave
P ~ Mbar
Direction of
SW propagation
Density, g/cm³
Ablator, $(C_8H_8)_n$ 25 μm
Probe
XFEL pulse:
7 keV, ~ 8 fs,
FWHM ~ 600 μm
Optical laser driver:
10-20 J, 5 ns
250 μm on target

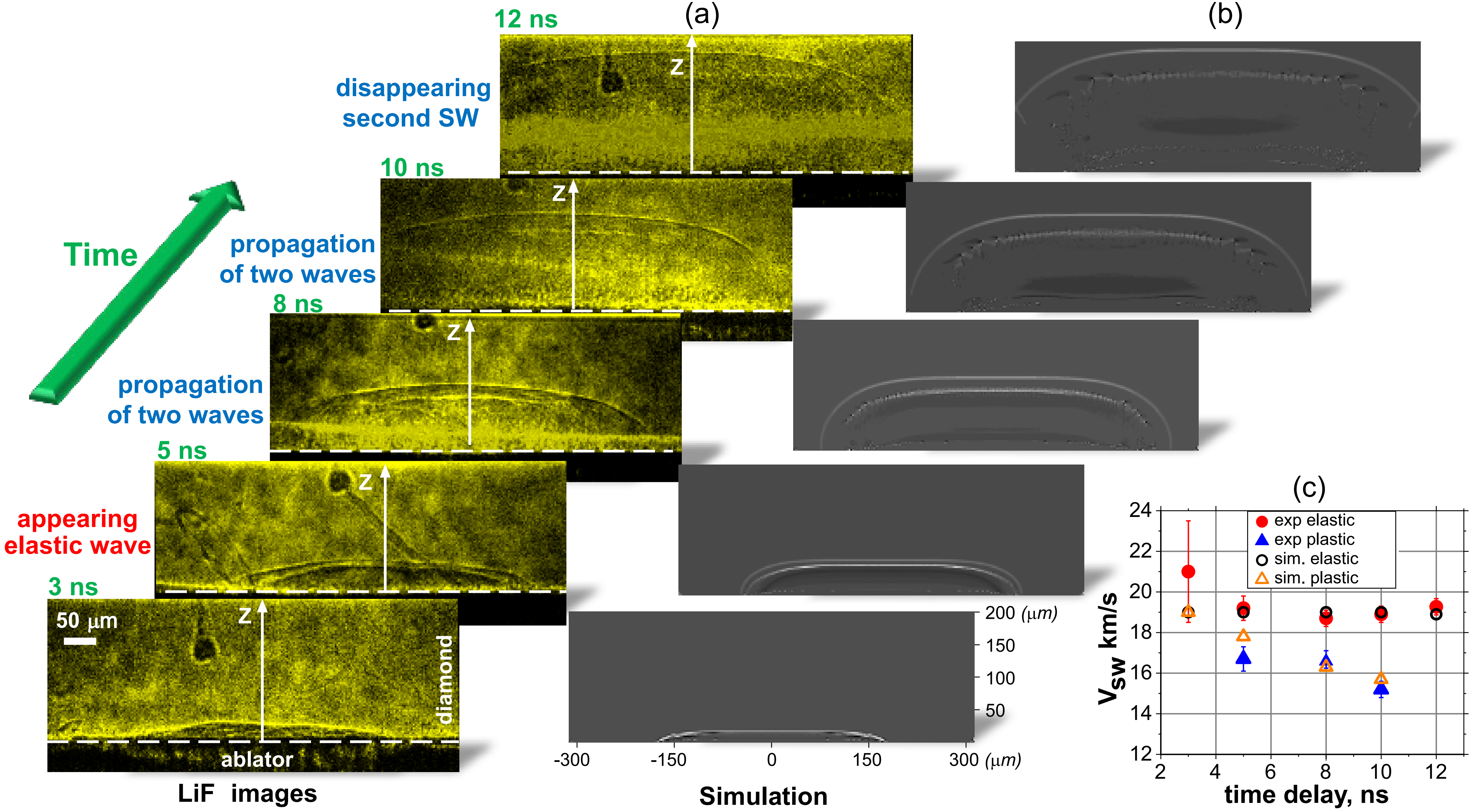
(a)
(b)
(c)
Time
12 ns
disappearing second SW
10 ns
propagation of two waves
8 ns
propagation of two waves
5 ns
appearing elastic wave
3 ns
50 μm
Z
diamond
ablator
LiF images
Simulation
200 (μm)
150
100
50
-300
-150
0
150
300 (μm)
● exp elastic
▲ exp plastic
○ sim. elastic
△ sim. plastic
V_{SW} km/s
24
22
20
18
16
14
12
2
4
6
8
10
12
time delay, ns

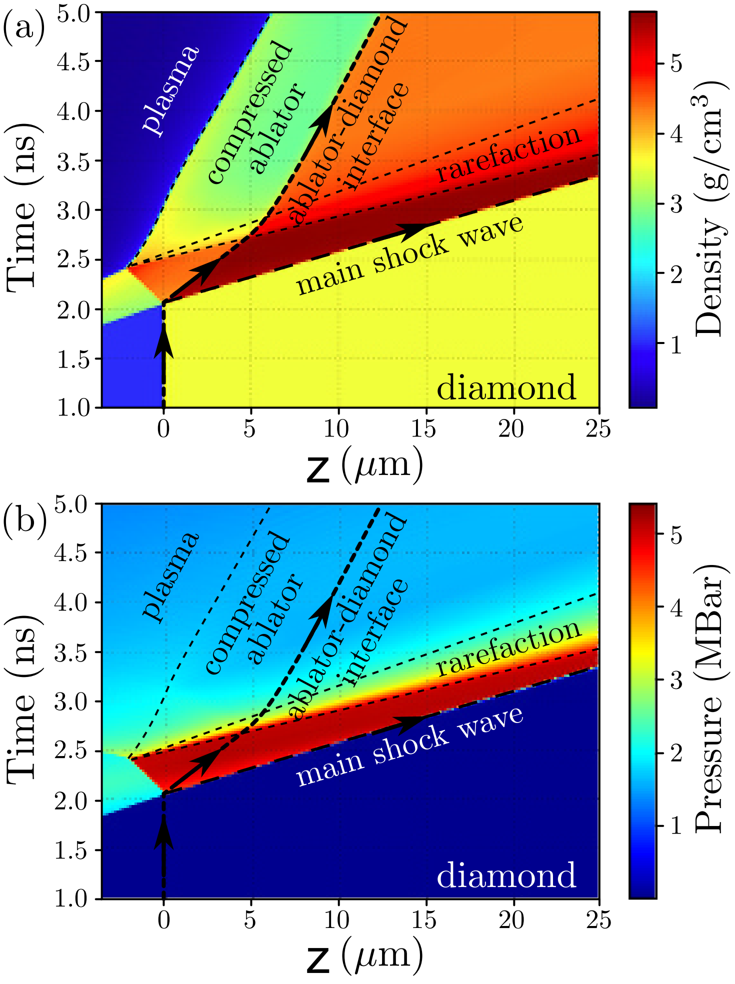
(a)
5.0
4.5
4.0
3.5
3.0
2.5
2.0
1.5
1.0
Time (ns)
0
5
10
15
20
25
z (μm)
plasma
compressed ablator
ablator-diamond interface
rarefaction
main shock wave
diamond
Density (g/cm^3)
1
2
3
4
5
(b)
5.0
4.5
4.0
3.5
3.0
2.5
2.0
1.5
1.0
Time (ns)
0
5
10
15
20
25
z (μm)
plasma
compressed ablator
ablator-diamond interface
rarefaction
main shock wave
diamond
Pressure (MBar)
1
2
3
4
5

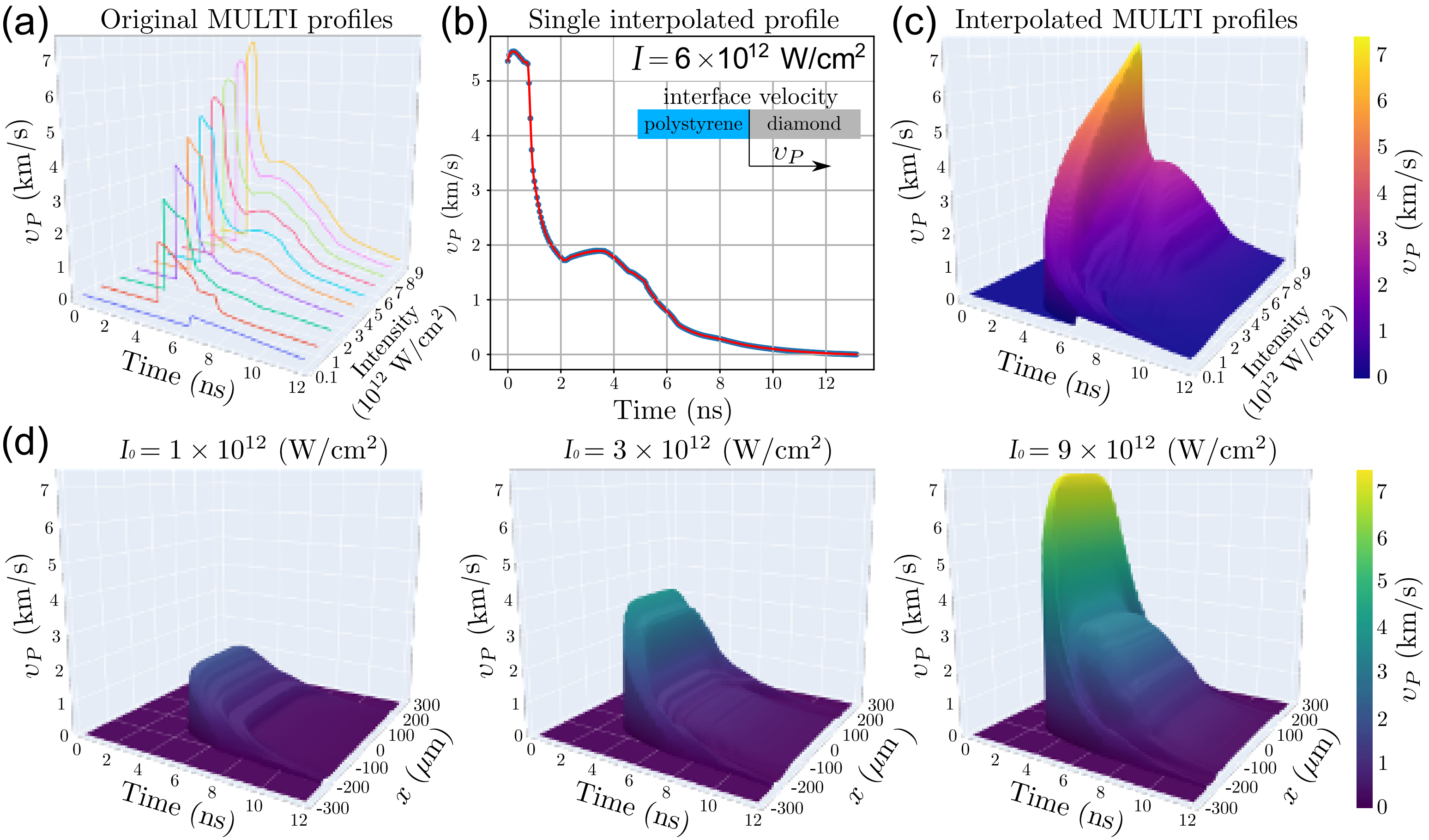
(a)
Original MULTI profiles
v_P (km/s)
Time (ns)
Intensity (10^{12} W/cm^2)
0.1 1 2 3 4 5 6 7 8 9
(b)
Single interpolated profile
$I = 6 \times 10^{12}$ W/cm^2
interface velocity
polystyrene
diamond
v_P
v_P (km/s)
Time (ns)
(c)
Interpolated MULTI profiles
v_P (km/s)
Time (ns)
Intensity (10^{12} W/cm^2)
(d)
$I_0 = 1 \times 10^{12}$ (W/cm^2)
$I_0 = 3 \times 10^{12}$ (W/cm^2)
$I_0 = 9 \times 10^{12}$ (W/cm^2)
v_P (km/s)
Time (ns)
x (μm)
300 200 100 0 -100 -200 -300

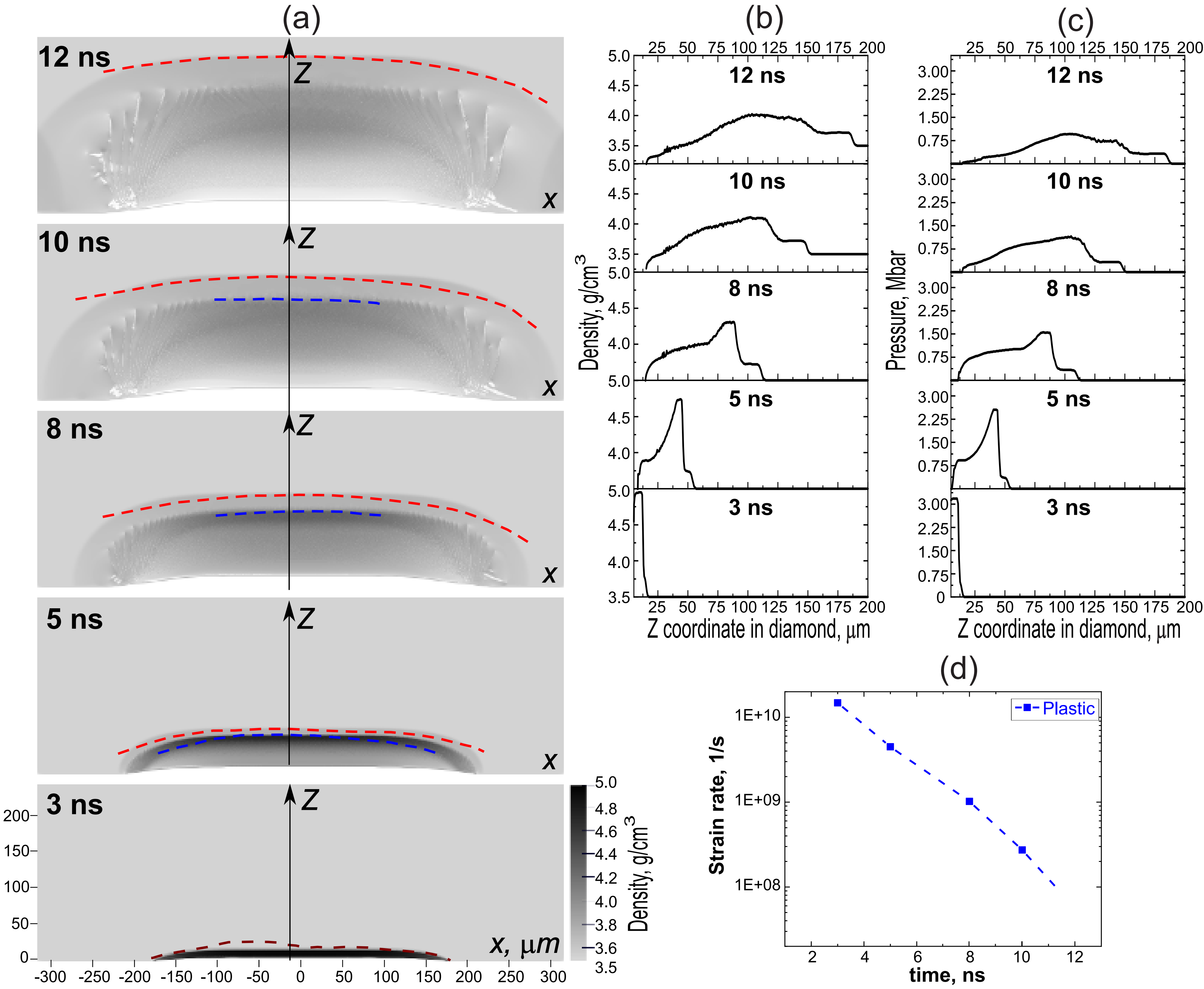
(a)
12 ns
10 ns
8 ns
5 ns
3 ns
Z
x
x, μm
-300 -250 -200 -150 -100 -50 0 50 100 150 200 250 300
0 50 100 150 200
Density, g/cm^3
3.5 3.6 3.8 4.0 4.2 4.4 4.6 4.8 5.0
(b)
Density, g/cm^3
Z coordinate in diamond, μm
25 50 75 100 125 150 175 200
3.5 4.0 4.5 5.0
(c)
Pressure, Mbar
Z coordinate in diamond, μm
0 0.75 1.50 2.25 3.00
(d)
Strain rate, 1/s
time, ns
1E+08 1E+09 1E+10
2 4 6 8 10 12
Plastic

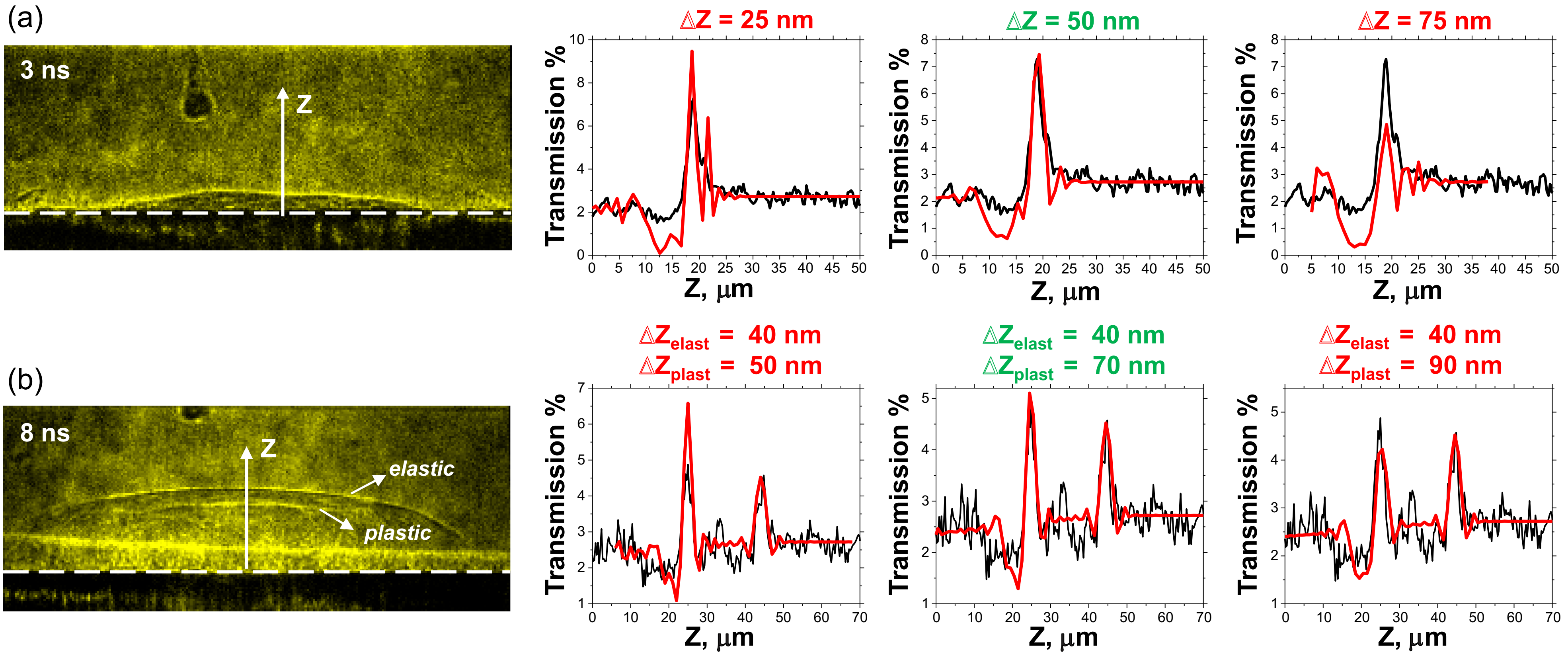
(a)
3 ns
Z
ΔZ = 25 nm
ΔZ = 50 nm
ΔZ = 75 nm
Transmission %
Z, µm
0 5 10 15 20 25 30 35 40 45 50
(b)
8 ns
Z
elastic
plastic
ΔZ_{elast} = 40 nm
ΔZ_{plast} = 50 nm
ΔZ_{elast} = 40 nm
ΔZ_{plast} = 70 nm
ΔZ_{elast} = 40 nm
ΔZ_{plast} = 90 nm
Transmission %
Z, µm
0 10 20 30 40 50 60 70

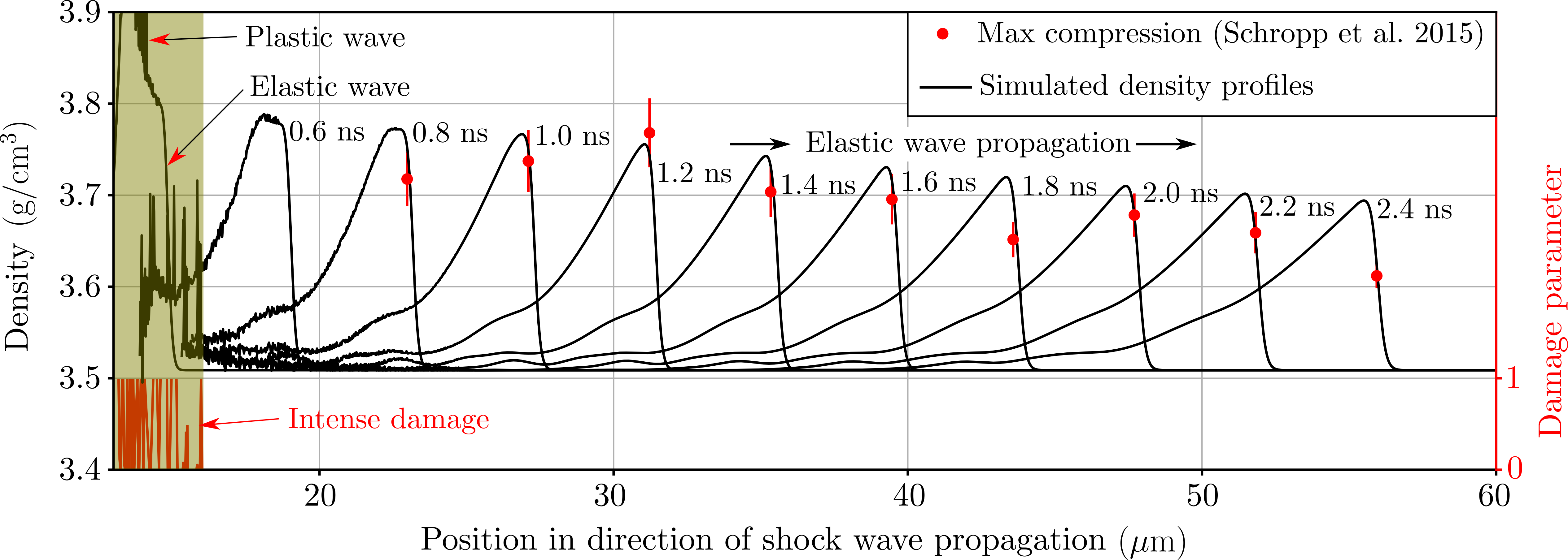
Plastic wave
Elastic wave
Intense damage
Max compression (Schropp et al. 2015)
Simulated density profiles
Elastic wave propagation
0.6 ns
0.8 ns
1.0 ns
1.2 ns
1.4 ns
1.6 ns
1.8 ns
2.0 ns
2.2 ns
2.4 ns
Density (g/cm^3)
3.9
3.8
3.7
3.6
3.5
3.4
Damage parameter
1
0
20
30
40
50
60
Position in direction of shock wave propagation (μm)

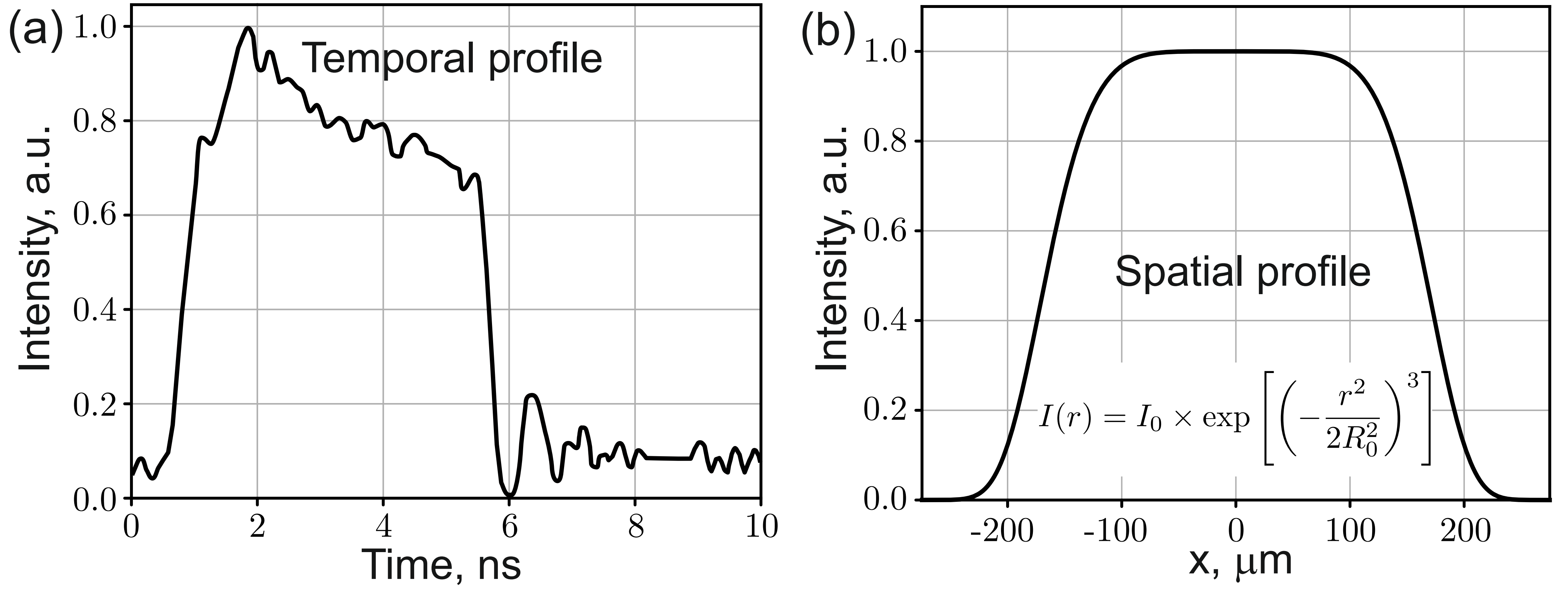
(a)
Temporal profile
Intensity, a.u.
1.0
0.8
0.6
0.4
0.2
0.0
0
2
4
6
8
10
Time, ns
(b)
Spatial profile
Intensity, a.u.
1.0
0.8
0.6
0.4
0.2
0.0
-200
-100
0
100
200
x, μm
$I(r) = I_0 \times \exp\left[\left(-\frac{r^2}{2R_0^2}\right)^3\right]$

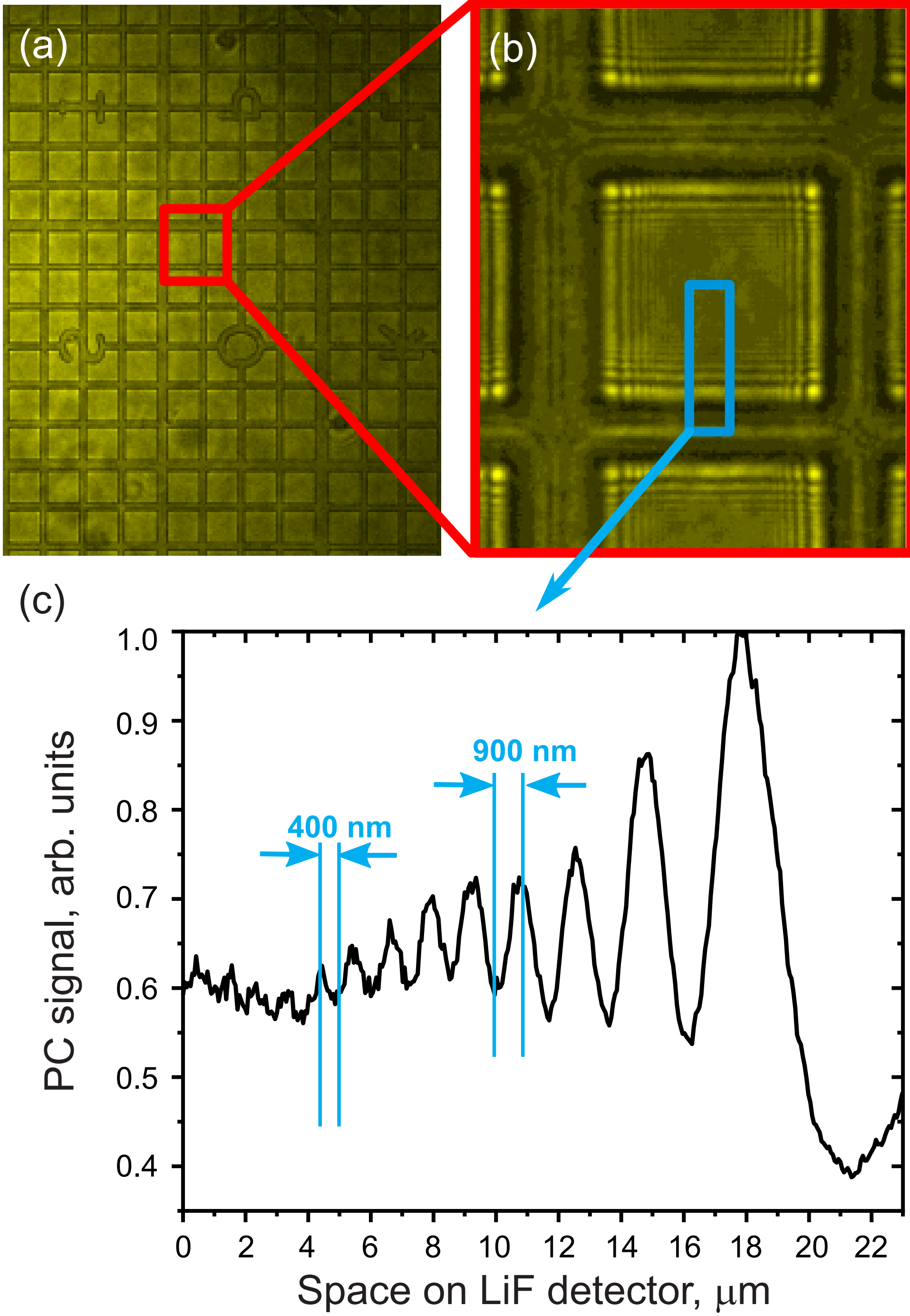
(a)
(b)
(c)
400 nm
900 nm
PC signal, arb. units
Space on LiF detector, μm
1.0
0.9
0.8
0.7
0.6
0.5
0.4
0
2
4
6
8
10
12
14
16
18
20
22

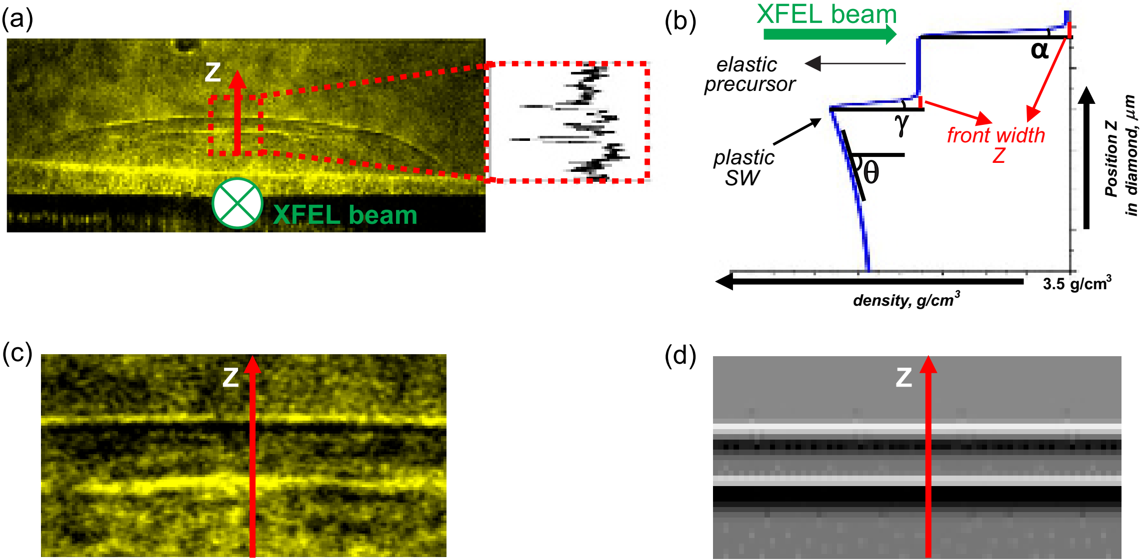
(a)
Z
XFEL beam
(b)
XFEL beam
elastic precursor
plastic SW
α
γ
θ
front width Z
Position Z in diamond, μm
3.5 g/cm³
density, g/cm³
(c)
Z
(d)
Z

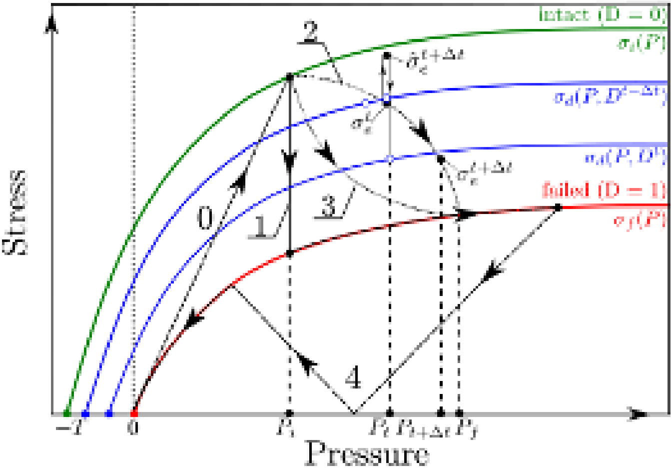
intact (D = 0)
$\sigma_i(P)$
$\hat{\sigma}_e^{t+\Delta t}$
$\sigma_d(P, D^{t-\Delta t})$
σ_e^t
$\sigma_d(P, D^t)$
$\sigma_e^{t+\Delta t}$
failed (D = 1)
$\sigma_f(P)$
2
0
1
3
4
Stress
$-T$
0
P_i
P_t
$P_{t+\Delta t}$
P_f
Pressure

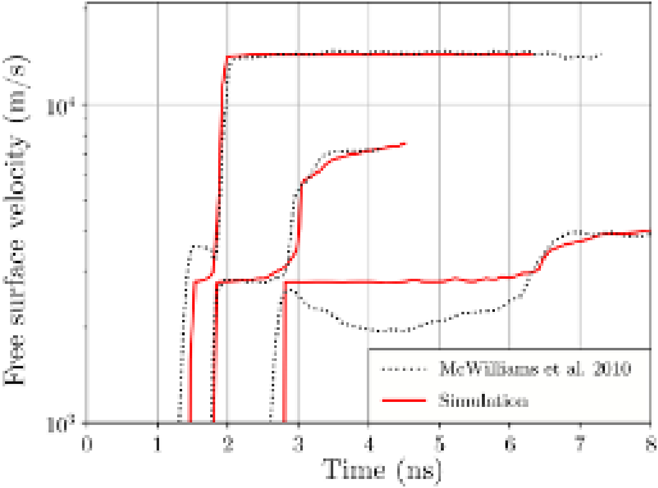

Free surface velocity (m/s)
10^4
10^3
0
1
2
3
4
5
6
7
8
Time (ns)
McWilliams et al. 2010
Simulation

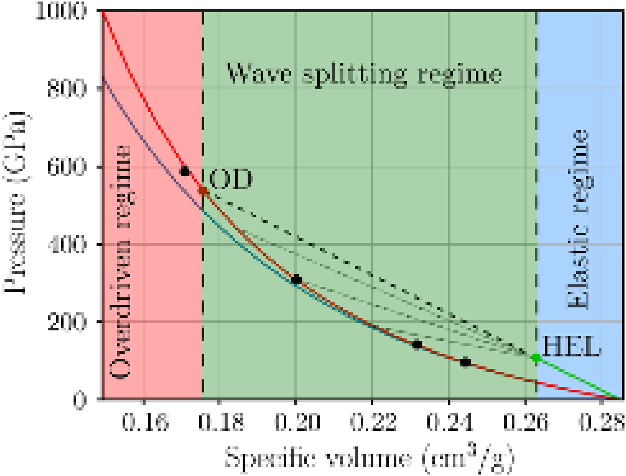
Wave splitting regime
Overdriven regime
Elastic regime
OD
HEL
1000
800
600
400
200
0
Pressure (GPa)
0.16
0.18
0.20
0.22
0.24
0.26
0.28
Specific volume (cm^3/g)

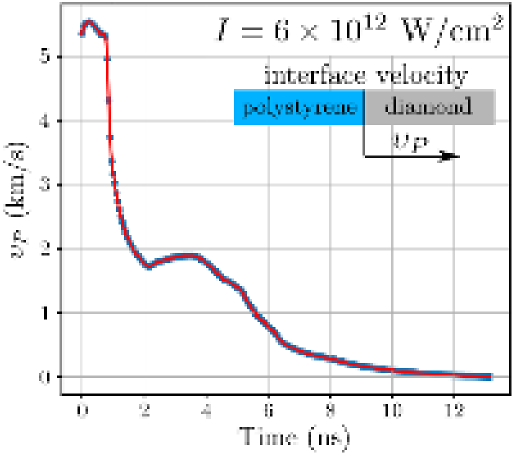

$I = 6 \times 10^{12}$ W/cm^2
interface velocity
polystyrene
diamond
v_P
v_P (km/s)
0
1
2
3
4
5
Time (ns)
0
2
4
6
8
10
12

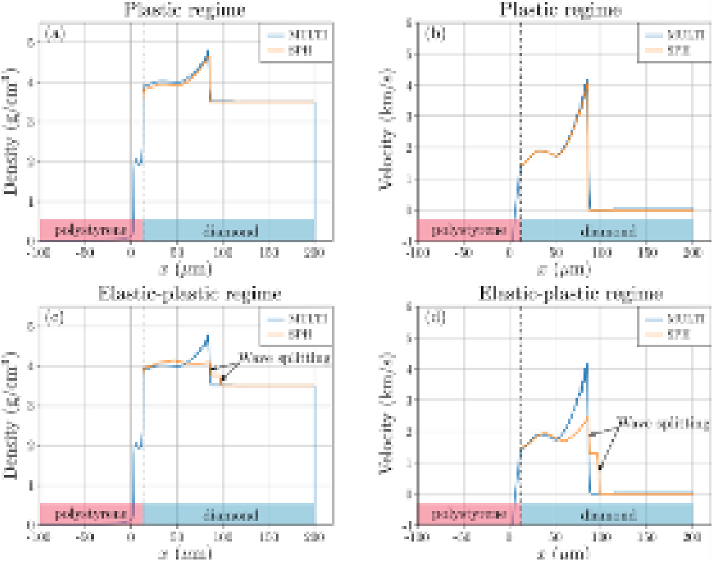
Plastic regime
(a)
Density (g/cm^3)
x (μm)
MULTI
SPH
polystyrene
diamond
Plastic regime
(b)
Velocity (km/s)
x (μm)
MULTI
SPH
polystyrene
diamond
Elastic-plastic regime
(c)
Density (g/cm^3)
x (μm)
MULTI
SPH
Wave splitting
polystyrene
diamond
Elastic-plastic regime
(d)
Velocity (km/s)
x (μm)
MULTI
SPH
Wave splitting
polystyrene
diamond
-100
-50
0
50
100
150
200

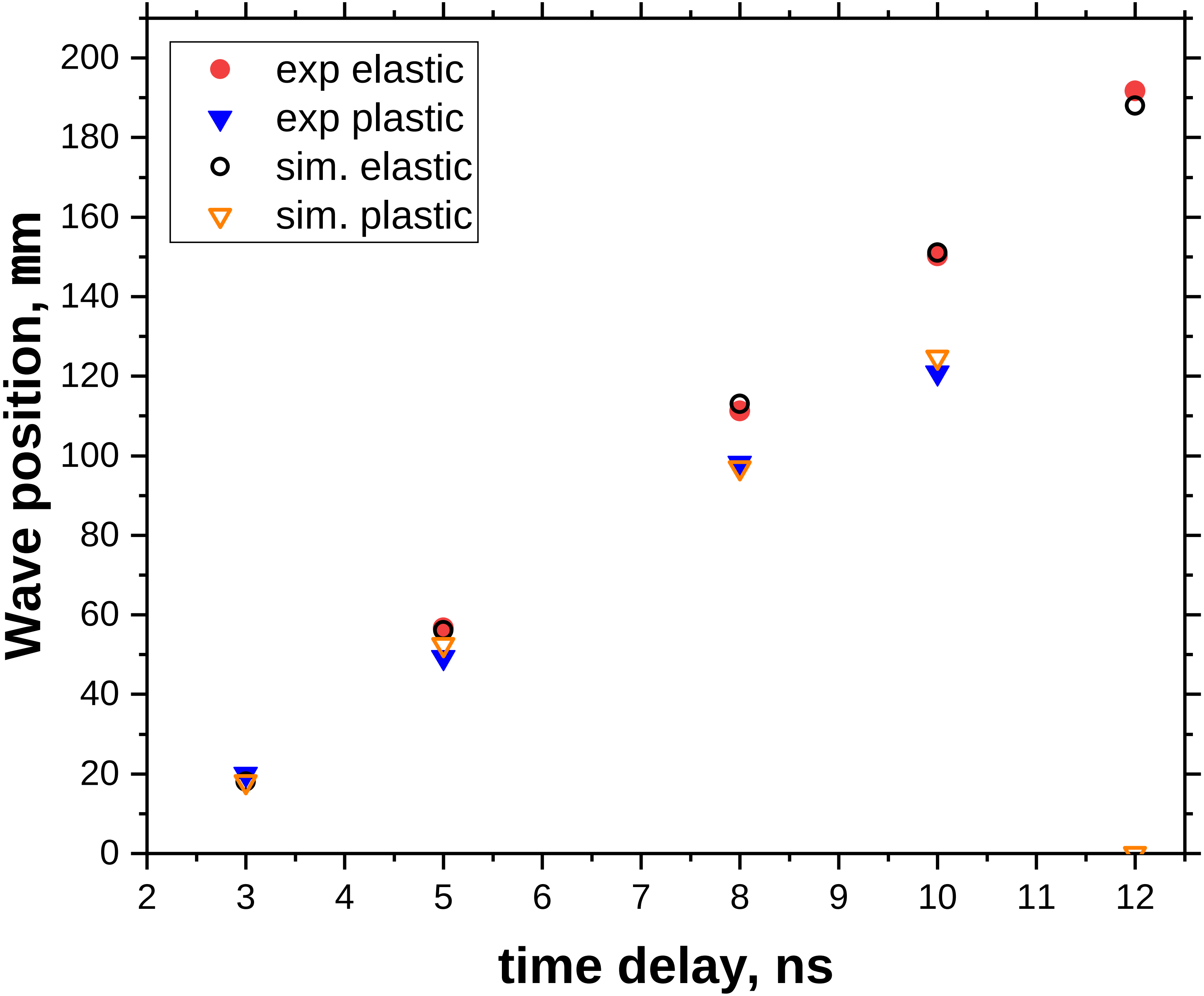
exp elastic
exp plastic
sim. elastic
sim. plastic
Wave position, mm
time delay, ns
0
20
40
60
80
100
120
140
160
180
200
2
3
4
5
6
7
8
9
10
11
12

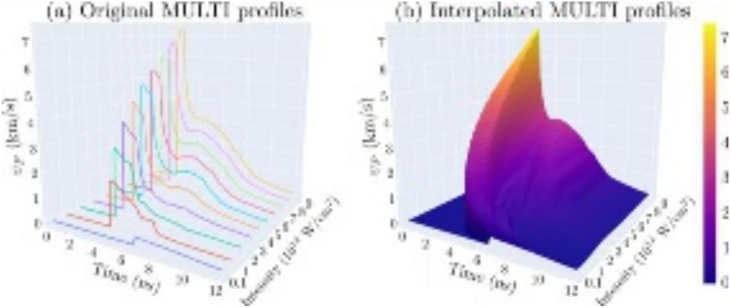

(a) Original MULTI profiles

(b) Interpolated MULTI profiles

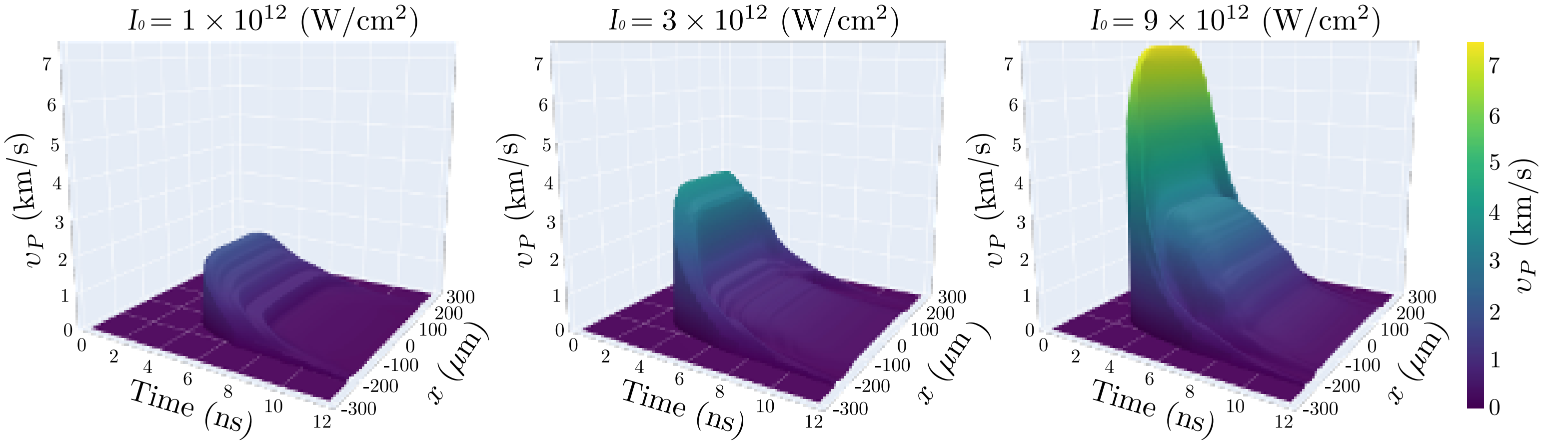
$I_0 = 1 \times 10^{12}$ (W/cm^2)
$I_0 = 3 \times 10^{12}$ (W/cm^2)
$I_0 = 9 \times 10^{12}$ (W/cm^2)
v_P (km/s)
0
1
2
3
4
5
6
7
Time (ns)
0
2
4
6
8
10
12
x (μm)
300
200
100
0
-100
-200
-300

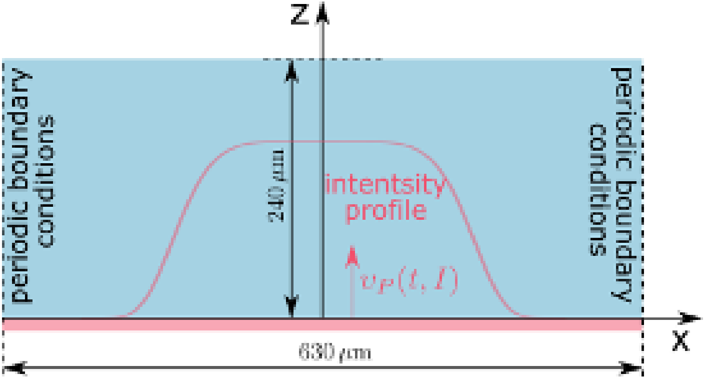
Z
periodic boundary conditions
240 μm
intentsity profile
$v_P(t, I)$
periodic boundary conditions
X
630 μm

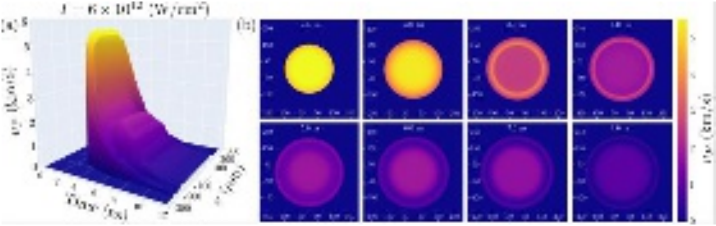
$I = 6 \times 10^{12}$ (W/cm^2)
(a)
(b)
Time (ns)
v_z (km/s)